

Statistical Mechanics on the Random Locally Tree-like Layered Lattice

A Thesis

submitted to

Indian Institute of Science Education and Research Pune

in partial fulfillment of the requirements for the

BS-MS Dual Degree Programme

by

Suman Satish Kulkarni



Indian Institute of Science Education and Research Pune

Dr. Homi Bhabha Road,
Pashan, Pune 411008, India.

July, 2021

Supervisor: Dr Deepak Dhar

TAC: Dr Kedar Damle

© Suman Satish Kulkarni 2021

All rights reserved

Certificate

This is to certify that this dissertation entitled 'Statistical Mechanics on the Random Layered Locally Tree-like Lattice' towards the partial fulfilment of the BS-MS dual degree programme at the Indian Institute of Science Education and Research, Pune represents work carried out by Suman Satish Kulkarni at Indian Institute of Science Education and Research under the supervision of Dr Deepak Dhar, Professor, Department of Physics, during the academic year 2020-2021.

Deepak Dhar
June 3, 2021
Dr Deepak Dhar

Committee:

Dr Deepak Dhar

Dr Kedar Damle

This thesis is dedicated to my mother.

*Those we love don't go away
They walk beside us everyday
Unseen, unheard but always near
So loved, so missed and very dear.*

Declaration

I hereby declare that the matter embodied in the report entitled 'Statistical Mechanics on the Random Layered Locally Tree-like Lattice', are the results of the work carried out by me at the Department of Physics, Indian Institute of Science Education and Research, Pune, under the supervision of Dr Deepak Dhar and the same has not been submitted elsewhere for any other degree.

Suman Kulkarni
3.06.2021
Suman Satish Kulkarni

Acknowledgments

I would like to express my deepest gratitude to my supervisor Prof. Deepak Dhar. For all the physics he has taught me. For the great amount of time and effort that he has invested into making me a better researcher. For his wisdom and wit. Thank you, Prof. Dhar for believing in me and constantly nudging me to aim higher. Our conversation right after you signed this thesis is something that I will always keep in mind and promise to work towards everyday.

I thank Prof. Kedar Damle for his contagious enthusiasm, for his guidance throughout this year, and for his questions and comments that made me learn and improve my work. Our group meetings were always tremendous fun and something that I eagerly looked forward to each week. It has been an absolute honour to be mentored by Prof. Dhar and Prof. Damle and my only hope is that at the end of this, I have inherited even a small fraction of their intuition, rigour and awesomeness. I would also like to thank my previous collaborator Dr. Collin Capano for his mentorship and encouragement in the past two years.

I thank my father for supporting (or rather bearing with?) me through thick and thin. A considerable part of this thesis was done at home, and I am grateful that he can be easily bullied into making me as many cups of ginger tea as I want. Thanks to my wonderful friends — Aagam, Aanjaneya, Adarsh, Adithya, Arya, Danish, Durgesh, Onkar, Sandip, Shriya and Vishrut ¹ — for making each day a little more interesting. My dearest friends Danish Pannu, Sandip George and Onkar Sadekar have always stood by me and had my best in mind.

These five years have been a period of immense growth. Thank you, IISER Pune.

¹its in alphabetical order, guys

Abstract

This thesis defines a variation of a regular random graph called the Random Locally Tree-like Layered Lattice (RLTL). Such lattices are of interest because the Bethe approximation becomes asymptotically exact on them. Unlike the usual Bethe lattice, the RLTL is finite and can be studied numerically. This makes studying problems in statistical physics on the RLTL more tractable. We study the geometrical structure of this graph and the behavior of the Ising model on it. Under the geometrical structure, we explore the properties of the diameter and the radius of gyration of this graph, study the r dependence on the average number of distinct sites present at distance r from a site and also look at the average length shortest loop passing through a site. We find that the average diameter of an r -regular RLTL is of order $[\log_{r-1}(S)]$ to leading order in S , where S is the total number of sites in the graph. The radius of gyration of the RLTL was also found to be linear in $\log(S)$. We then look at the Ising model on the RLTL and look at the finite-size scaling on the lattice. The finite-size effects of the Ising model on random graphs is not well studied in previous literature. On the RLTL, we study the finite-size scaling for the magnetic susceptibility (χ) and deviations in the specific heat capacity from the theoretical value (ΔC_v). We find that the magnetic susceptibility per site obeys a scaling of the form $\chi = S^{1/2} f(\epsilon S^{1/2})$ and the deviations in the specific heat has a scaling of the form $\Delta C_v = g(\epsilon S^{1/2})$, where $\epsilon = (T - T_c)/T_c$. We propose a theory which explains the observed scaling and explicitly calculate the exact scaling functions.

Contents

Abstract	xi
1 Introduction	5
2 Geometrical properties of the RLTL	9
2.1 Diameter	15
2.2 Radius of Gyration	22
2.3 Study of sites at distance r from a point	23
2.4 Four coordinated RLTL	27
2.5 Shortest loop passing through a point	29
3 The Ising Model on the RLTL	35
3.1 Ising model on the Bethe lattice	36
3.2 Monte Carlo studies of the Ising model on the RLTL	45
3.3 Finite-size scaling on the RLTL	53
3.4 Theory for finite-size scaling of the Ising model on the RLTL	55
3.5 Corrections to scaling	61
4 Summary	63

List of Figures

1.1	A Cayley tree with $n = 3$ shells	6
2.1	A realization of the three-coordinated RLTL with $m = 3$ bilayers and $N = 2^m$ sites per layer.	10
2.2	Short loops of size 2 and 4 on the three-coordinated RLTL.	11
2.3	Possible loops of size 6 passing through a random site O on the three-coordinated RLTL.	12
2.4	Possible loops of size 8 passing through a random site O on the three-coordinated RLTL	13
2.5	Locally tree-like property of the RLTL.	14
2.6	Sample-averaged diameter as a function of $\log_2(N)$ for the three-coordinated RLTL	16
2.7	Sample-averaged diameter as a function of $\log_2(S)$ for the three-coordinated RLTL	17
2.8	Studying Bollobas' upper bound on the diameter of r -regular random graphs: Sample-averaged diameter as a function of $\log_{r-1}(2.rS.\log(S))$ for the three-coordinated RLTL ($r = 3$)	18
2.9	Probability distribution of the diameter of the RLTL across different realizations for $m = 2$ bilayers	19
2.10	Understanding the step-like structure of the diameter plots: sample-averaged diameter vs $\log_2(S)$ for an RLTL with $m = 4$ along with error bars	19

2.11	Understanding the step-like structure of the diameter plots: sample-averaged standard deviation of the diameter as a function of $\log_2(S)$ for the three-coordinated RLTL with $m = 4$	20
2.12	Probability distribution of the furthest distance possible from a site for the three-coordinated RLTL with $m = 2$	21
2.13	Studying the clustering of sites on the RLTL	21
2.14	Sample-averaged radius of gyration (R_{gyr}) as a function of $\log(S)$	22
2.15	Fraction of sites within the r^{th} shell averaged over extremal sites compared to the average over all sites in the lattice	24
2.16	Ratio of the fraction of sites within the r^{th} shell surrounding a point averaged over all sites (P_{all}) to that of extremal sites ($P_{extremal}$) as a function of r for a fixed value of $S = 2400$. Each data point is sample-averaged over 100 realizations of the RLTL.	24
2.17	Sample-averaged probability that the distance between two randomly picked sites is greater at R as a function for R for the RLTL with a single bilayer $m = 1$. Each data point is averaged over 100 independent realizations of the RLTL.	26
2.18	Logarithm of the probability that two randomly chosen sites on the RLTL are at a distance greater than R from each other as a function of R for lattices with a single bilayer. The curves are then fitted to the form given in Eq.2.7. We find that value of a to be ~ 1.58	27
2.19	Constructing the 4-coordinated RLTL (shown: the first two steps without the boundary conditions).	28
2.20	Sample-averaged diameter as a function of $x = \log_{r-1}(2.rS.\log(S))$ for the four-coordinated RLTL where $r = 4$. Each data point is averaged over 200 independent realizations of the RLTL. The dotted line denotes the bound given by Bollobas in Eq. 2.3	29
2.21	Distribution of the size of the average shortest loop passing through a site on RLTLs with fixed M . Each data point is sample-averaged over 100 independent realizations.	30
2.22	Distribution of the size of the average shortest loop passing through a site on the RLTL for fixed N . Each data point is sample-averaged over 100 independent realizations.	31

2.23	Understanding the effects of the aspect ratio of the RLTL: study of the distribution of the shortest loop passing through a site for the three-coordinated (top panel) and four-coordinated RLTL (bottom panel) for a fixed number of total sites (S). Each data point is sample-averaged over 100 independent realizations.	32
2.24	Understanding the effects of the aspect ratio of the RLTL: study of the fraction of shortest loops passing through a site that wind around the three-coordinated RLTL in the transverse (m) direction. Each data point is sample-averaged over 100 independent realizations of the RLTL.	33
2.25	Understanding the effects of the aspect ratio of the RLTL: study of the fraction of shortest loops passing through a site that wind around the four-coordinated RLTL in the transverse (m) direction. Each data point is sample-averaged over 100 independent realizations of the RLTL.	34
3.1	A three-coordinated Cayley tree consisting of N levels centred at site O . . .	36
3.2	Site a at level r in the Cayley tree connected to two subtrees T_1 and T_2 below via sites b and c at level $r + 1$	37
3.3	Solutions to the recursion equation Eq. 3.3 for different values of x_0 . Note that the range of x_0 is $[-1,1]$	38
3.4	Effective field at a site on the Bethe lattice	39
3.5	Calculation of the energy per bond using the effective field due to the sub-trees.	40
3.6	Site σ' at a level r in the tree	41
3.7	Magnetization per site in the presence of external magnetic field.	42
3.8	Difference between the observed and theoretical values of the specific heat per site (ΔC_v) as a function of ε for the three-coordinated RLTL with a single bilayer.	45
3.9	Probability density distribution of the magnetization per site for RLTLs of size $S = 2^{13}$ and 2^{16} respectively. For $T \leq T_c$, the distribution of the magnetization has two peaks. For $T > T_c$, the distribution of the magnetization is a single peak centred around $m = 0$. As the size of the system increases, the peaks get sharper.	48

3.10	Energy per site as a function of temperature for the three-coordinated RLTL with a single bilayer for different values of N . The dashed line is the theoretically expected curve (given by Eq. 3.8). The vertical line denotes the critical temperature T_c . The maximum error bar is of order 10^{-4} for $N \geq 8$ and order 10^{-3} for $N < 8$	49
3.11	Absolute magnetization per site as a function of temperature for the three-coordinated RLTL with a single bilayer for different values of N . The dashed line is the theoretically expected curve for the Bethe lattice (given by Eq. 3.7). The vertical line is at the critical temperature T_c	50
3.12	Specific heat capacity per site as a function of temperature for the three-coordinated RLTL with a single bilayer for different values of N . The dashed line is the theoretically expected curve (given by Eq. 3.9). The vertical line is at the critical temperature T_c	51
3.13	Magnetic susceptibility per site as a function of temperature for the three-coordinated RLTL with a single bilayer for different values of N . The dashed line is the theoretically expected curve (given by Eq. 3.16 and 3.17). The vertical line denotes the critical temperature T_c	52
3.14	Scale factors used to collapse the peaks in the C_v and χ plots to the same point.	54
3.15	Scaling collapse for ΔC_v vs ε	54
3.16	Scaling collapse for χ vs ε	55
3.17	Scaling collapse for the magnetic susceptibility for the four-coordinated RLTL with a single layer.	56
3.18	Fitting the probability distribution of m to the Landau form in Eq. 3.24 for the three-coordinated RLTL. We obtain a value of $a = 0.29$ and $b = 0.02$. . .	57
3.19	First step of renormalization of a block of spins of size four on the three-coordinated RLTL.	57
3.20	Theoretical scaling function for the magnetic susceptibility.	61
3.21	Difference between the observed scaling function and the theoretical (asymptotic) scaling function at $\varepsilon S^{1/2} = -10$ as a function of N (recall that the number of sites per layer is 2^N). The dashed line is the function $S^{-1/2}$	62

Chapter 1

Introduction

Exact solutions to problems in statistical physics are not always possible. Hence, it is important to have approximation methods of wide applicability. The Bethe approximation is one such approximation technique [1]. Unlike the simple mean-field approximation which replaces the interactions with all neighbours by a single “mean field”, this method takes care of nearest-neighbour correlations between spins. It was then shown that the Bethe approximation becomes exact on an infinite regular tree — ie, a lattice in which each site has the same coordination number and has no loops. In particular, the authors in Ref. [2] studied the ferromagnetic Ising model on such a lattice and showed that the partition function obtained is exactly that of the Bethe approximation. This lattice is called the “Bethe lattice”.

At this point, it is important to understand the distinction between the Bethe lattice and a Cayley tree. A Cayley tree of coordination number q is a finite graph that is constructed as follows: Start with a single central root site O . To this, we connect q sites which form a part of the first “shell” around O . Subsequent shells are then constructed by adding $q - 1$ distinct sites to *each* site present in the previous shell ¹. This procedure is repeated until n shells are constructed. It is clear from the definition that this graph has no loops. However, the sites at the boundary (ie, on the n^{th} shell) have coordination number 1 and are thus different from the rest of the sites in the graph. Fig. 1.1 shows a Cayley tree with $n = 3$ shells.

¹From this construction, it is clear that the number of sites on the r^{th} shell from site O is $q(q - 1)^{r-1}$

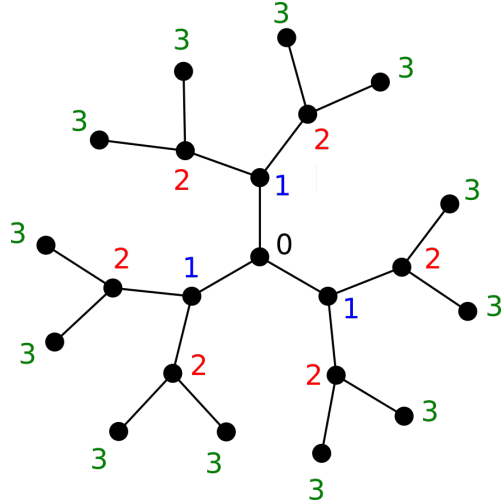


Figure 1.1: Cayley tree with $n = 3$ shells

The Bethe lattice on the other hand, is a tree in which all sites have the same coordination number (say q). This graph is infinite and has no notion of a central site or a boundary. The Cayley tree, unlike the Bethe lattice, has a large number of sites on the boundary which leads to a very different behaviour from the Bethe lattice. For example, the Ising model on the Cayley tree is known to display unusual properties [3]–[5]. The Ising model on the Bethe lattice has also been solved and a detailed treatment is given in Ref. [6].

Differences between these lattices aside, both the Bethe lattice and the Cayley tree are not easily usable to study methods in statistical physics. The Bethe lattice is not easily accessible to numerical techniques. The Cayley tree on the other hand has a very large number of sites on its boundary. Unlike usual d -dimensional regular lattices, the ratio of the number of sites at the boundary to the total number of sites for this graph does not approach zero in the thermodynamic limit. The Cayley tree is thus very sensitive to the boundary conditions. Obtaining the properties of the bulk involves a procedure of careful subtraction to remove the surface effects, which makes problems difficult.

It was later realized that random regular graphs provide a more convenient setting to study the Bethe approximation [7]–[10]. Random graphs, of course, have been a subject of extensive study in graph theory [11]–[14]. The books listed in Refs. [15] and [16] contain a comprehensive summary on the theory of random graphs. In particular, given a k -regular random graph of total number of sites S , it can be shown that the expected number of short loops of length l goes as $(k - 1)^l$ [15]. In the limit of large S , the fractional number of short

loops of length $l < \log(S)$ goes to zero. If we pick any site in this random graph, this means that upto a distance of $\mathcal{O}[\log S]$, the graph locally looks as though it is branching out — ie, it is locally “tree-like”. So, in this large S limit, the graph looks like the Bethe lattice. Since these graphs are regular, they avoid the problem of surface corrections altogether which makes studying problems on these lattices more tractable by simulations.

The Random Locally Tree-Like Layered Lattice (RLTL) is a variation of a random regular graph. It has additional structure which allows the use of techniques like the transfer matrix method. The RLTL was first introduced in Ref. [17] as a way to study the Bethe approximation for a system of hard rods. In this thesis, we work with a modification of this lattice, details of which are described in Chapter 2. We also explore the geometrical structure of this lattice in this chapter. We then use the properties of this lattice to understand the behaviour of the Ising model on this lattice in Chapter 3. In particular, we study the finite-size corrections to the thermodynamic limit of regular random graphs. We argue that near the critical point, the free energy is of the form given by Landau theory and use this to explicitly calculate the exact finite-size scaling functions. These results are then verified numerically using Monte-Carlo simulations. While the Ising model on random graphs and complex networks has been studied previously (see for example [8], [18]–[20]), the finite-size effects of random graphs has not been studied well in previous literature.

Chapter 2

Geometrical properties of the RLTL

In this chapter, we define the Random Locally Tree-Like Layered Lattice (RLTL) along the lines of the lattice introduced in Ref. [17] with some modification. We then study the geometrical structure of the RLTL. Some understanding of these properties is a prerequisite for a detailed study of various models on the lattice.

Three-coordinated RLTL

We start out by describing the construction of the RLTL in the simplest setting: that of coordination number three. This lattice consists of sites arranged in *bilayers* with equal number of sites in each layer. We denote the number of bilayers by m and the number of sites in each bilayer as N . The total number of sites in the lattice is denoted $S = 2mN$. Sites within each layer are labelled from 1 to N . Edges between these sites are then constructed using the following description:

1. Within each bilayer — i.e., between the $(2j + 1)^{th}$ and $(2j + 2)^{th}$ layer — we add a set of $2N$ bonds: The site i on layer $(2j + 1)$ is connected to site i and $(i + 1)$ on layer $(2j + 2)$. Periodic boundary conditions are imposed in the lateral direction and so, site N in layer $(2j + 1)$ is connected to site 0 in layer $(2j + 2)$. Each bilayer thus forms a single loop. We will refer to the bonds between sites within each bilayer as the zig-zag bonds (shown as the black edges in the example provided in Fig. 2.1).

2. Between the bilayers (i.e., between layer $2j$ and $2j + 1$), we add N bonds which are constructed after performing random permutations. First, we construct a random permutation σ on the labels 1 to N , where $\sigma[i]$ denotes the new label of site i . Then, we connect site i on layer $2j$ to site $\sigma[i]$ on layer $2j + 1$. The permutation for each j is chosen independently. Finally, we impose periodic boundary conditions in the transverse direction: the sites in the last layer are connected to sites in the first layer via random permutations. We will refer to the bonds between sites on adjacent bilayers as inter-layer bonds (shown as the red edges in the example provided in Fig. 2.1).

We note that this lattice is by definition bipartite and hence does not have any loops of odd length. For a lattice with m bilayers, a set of m *independent* permutations on the sites 1 to N $\{\sigma_1, \dots, \sigma_m\}$ gives us *one* particular realization of the RLTL. Fig. 2.1 shows an example of a realization of the RLTL graph with $m = 3$ bilayers and $N = 2^3$ sites per layer (bonds arising due to the periodic boundary conditions are not shown). Thus, to understand the behaviour of any quantity on the RLTL, we must average over different realizations of the lattice. We will show subsequently in this chapter however, that given a particular value of (m, N) , the behaviour of different quantities of interest shows only small variations across different realizations.

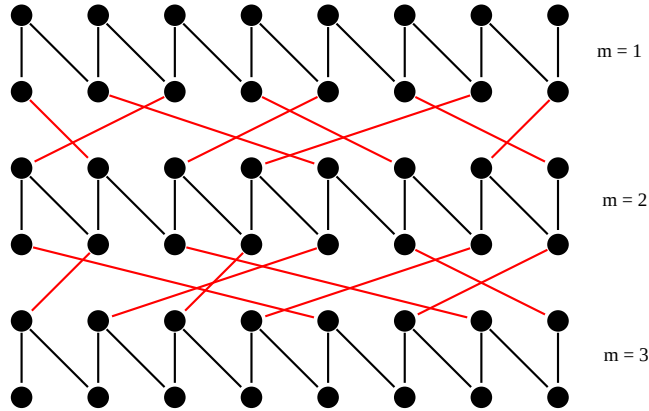


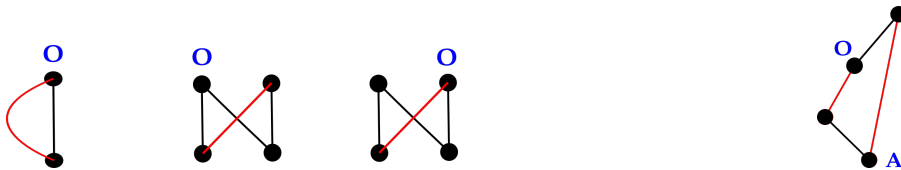
Figure 2.1: A realization of the RLTL with $m = 3$ bilayers and $N = 2^m$ sites per layer. Sites within the same bilayer are connected via zig-zag lines (shown as the black edges). Sites in adjacent bilayers are then connected via random permutations (shown as the red edges). The lattice is periodic in the transverse and longitudinal direction (not shown).

2.0.1 Locally tree-like property:

A key property of the RLTL which makes it useful when studying problems in statistical physics is that in the limit of large N , the lattice locally looks like a tree. This is because there are very few short loops in this limit. If there are no loops of size less than or equal to $2l$ passing through any randomly picked site, then upto a distance l from a site, the lattice locally appears to branch out and cannot be distinguished from a uniform tree. We then say that this graph has a “locally” tree structure (see Fig. 2.5a).

To understand this locally tree-like property and how likely short loops are on the RLTL, we look at the probability that any random site O on this graph has a short loop of a given size passing through it. In all our calculations, we shall only consider the terms of leading order and ignore terms involving the subtraction of any overlapping configurations. We also ignore lattices which have a very small N where the bilayer itself forms a short loop.

Without loss of generality, we can choose site O to be on the bottom of a bilayer. If instead we were to take O to be on top of a bilayer, the arguments can be made on similar lines and the answers would not change. As noted earlier, this lattice is bipartite and therefore has no loops of odd length. It is also clear from the construction, that for $m > 1$ there are no loops of size two passing through O and for $m > 2$, there are no loops of size four passing through O .



(a) Loops of size 2 and 4 passing through O for RLTLs with a single bilayer. Each figure occurs with a probability $1/N$. (b) Loop of size 4 passing through O for RLTLs with two bilayers. This loops occurs with probability $2/N$

Figure 2.2: Short loops of size two and four which only occur on the three-coordinated RLTL with $m \leq 2$

Loops of length two and four arise due to the inter-layer bonds formed because of periodic boundary conditions in the transverse direction. For the case of a single bilayer $m = 1$, the possible loops of these sizes passing through O are shown in Fig. 2.2a. Since inter-layer bonds are constructed by random permutations, the probability that any two given sites

present on adjacent bilayers are connected by an inter-layer bond is $1/N$. The probability that there is a loop of size two and four passing through O is then $1/N$ and $2/N$ respectively.

For RLTLs with $m = 2$, the smallest possible loop passing through O is of size 4 which happens as shown in Fig. 2.2. The probability that site O has such a loop is $2/N$ since site A can connect to either of the two sites in the layer above O that are connected to O .

From here on we restrict ourselves to loops which do not involve bonds arising due to periodic boundary conditions in the transverse direction. Fig. 2.3 shows the possible loops of size six passing through site O . Each of these loops occur with a probability $2/N$ — since the site on the same layer as O can connect to a site either to the left or to the right of the site connected to O via an inter-layer bond (and each of these occur with a probability $1/N$). So, the probability that site O has a loop of size six passing through it is $6/N$.

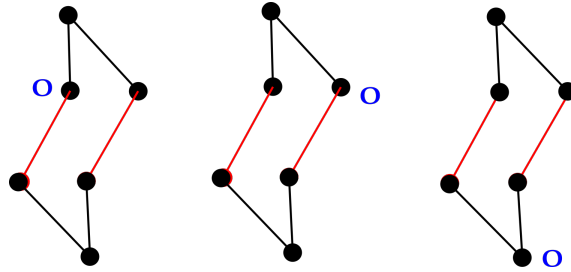


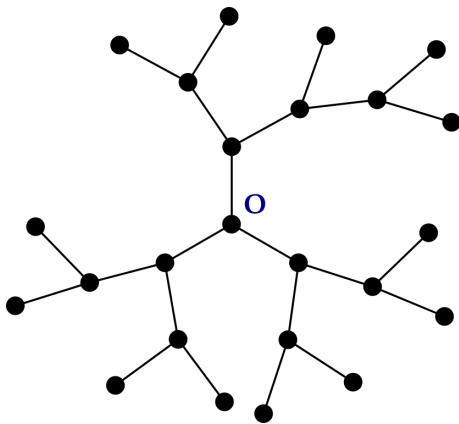
Figure 2.3: Possible loops of size 6 passing through site O . The probability of each configuration is $2/N$. Hence, the probability that site O is part of a loop of size 6 is $6/N$.

Similarly, it can be shown that the probability that O is part of a loop of size eight is $16/N$ as each of the loops shown in Fig. 2.4 occurs with probability $2/N$.

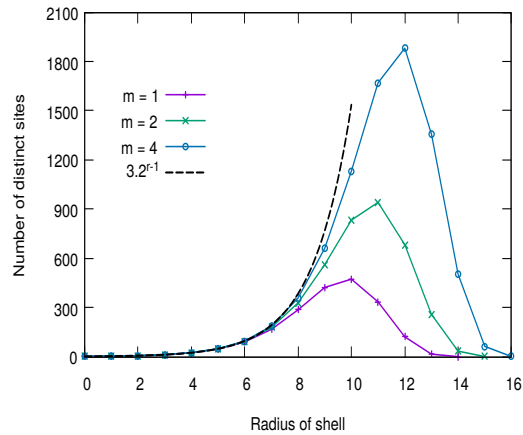
Using the above results, the average number of loops of size 6 and 8 on the RLTL is $2m$ and $4m$ respectively. Recall that we have not considered loops that have edges that were constructed as a result of periodic boundary conditions in the transverse direction. Such loops also occur with a finite probability that is proportional to $1/N$ (i.e., they will be of the form k/N where k remains finite even when N tends to infinity). In the limit of large N then, the *fractional* number of loops of short size tends to zero. Said differently, if we pick any random site on the graph and study its neighbourhood, it is very unlikely that there will be a short loop passing through it. The region around this site then looks like a tree as shown in Fig. 2.5.

Upto what distance from a site does this locally tree-like property hold? We can make

In Fig. 2.5b, we plot the average number of distinct sites present on the r^{th} shell around a site on the RLTL and the Bethe lattice. If there were no loops on the RLTL, the number of sites in the r^{th} shell would be $3 \cdot 2^{r-1}$, as expected on the Bethe lattice. However, the presence of loops of length $2l$ reduces the number of distinct sites present on the l^{th} shell. We see that upto a distance of $\mathcal{O}[\log_2 N]$, the number of distinct sites present in the r^{th} shell



(a) Site O does not have short loops passing through it and hence locally the graph looks like a branching out tree.



(b) The number of distinct sites present in the r^{th} shell surrounding a point O for an RLTL with $N = 1000$.

Figure 2.5: Locally tree-like property of the RLTL.

around a point follows the curve that we expect on the three-coordinated Bethe lattice — consistent with the locally tree-like property. Beyond that, there are deviations because of the presence of longer loops in the lattice.

While we have argued that the RLTL has a local tree-like structure, this property is in general asymptotically true for all regular random graphs. It was shown by Bollobás [15] that the number of short loops of size l on an r -regular random graph is an asymptotically Poisson distributed random variable with mean $(r-1)^l/2l$, and that the distributions for different l are independent of each other. The expected number of loops of size l thus remains finite even when the total number of sites in the graph is large and so, in this limit, the *fractional* number of short loops tends to zero, and the immediate neighbourhood around a site appears to be like a tree.

We now turn our attention to quantifying length scales associated with the RLTL.

2.1 Diameter

The distance between any two pairs of sites u and v in a graph is the number of edges present in the shortest path connecting u and v . Let us denote this as $d(u, v)$. Since the graph we are studying is undirected, this distance is symmetric in pairs of sites — ie, $d(u, v) = d(v, u)$.

The diameter of the graph is defined to be the maximum possible distance between any two pairs of sites in the graph:

$$D = \max_{u \in V, v \in V} d(u, v)$$

The behavior of the diameter of graphs — in particular that of regular random graphs — is an old and well studied problem [15], [21]–[23]. Ref. [24] and [25] provide a good survey of known results in the context of diameters of graphs; the latter also highlights some interesting open problems and directions. For the RLTL, we expect the average diameter to be of order $\log S$ (considering only terms that are leading order in S).

We can obtain a simple lower bound on the diameter of the RLTL. This inequality is due to Erdős [11], [26] and holds for all regular graphs. It is known that for the three-coordinated Bethe lattice, the number of distinct sites present at distance r from a point is $3 \cdot 2^{r-1}$. So, the number of sites *within* distance r is:

$$N(R) = 1 + \sum_{r=1}^R 3 \cdot 2^{r-1} = 3 \cdot 2^R - 2$$

By definition, all sites in a (finite and connected) graph are within a distance D from each other. Further, since the RLTL has loops, the number of distinct sites within distance R from a point will be lower than the corresponding number on the Bethe lattice. This means that $S \leq N(D)$, which gives us:

$$D \geq \log_2 \left(\frac{S+2}{3} \right) \tag{2.2}$$

An upper bound on the diameter of regular random graphs was obtained by Bollobás and Vega in Ref. [26]. Consider an r -regular random graph on S sites. Let ε be a fixed positive

constant and d be the least integer satisfying

$$(r - 1)^{d-1} \geq (2 + \varepsilon) r S \log S \tag{2.3}$$

It was then shown by Bollobás and Vega that almost every r -regular random graph of size S has a diameter *at most* d .

From these two bounds on d , we expect that the diameter of the RLTL graph to be of $\mathcal{O}[\log_{(r-1)} S]$. This would generally be true for all regular random graphs.

We test this out by numerically studying of the sample-average diameter of the RLTL. Since the RLTL has loops, we stick to finding the diameter by brute force. We first find the maximum furthest distance possible from each site in the lattice and then take the maximum value of this over all the sites. To find the furthest distance possible from a site v , we construct a breadth-first traversal tree starting from v which terminates when all sites in the lattice have been covered. The depth in the tree at which this occurs gives the maximum distance possible from v . We then repeat this for all the sites in the lattice; the maximum value over all sites is the diameter. Finally, we calculate the diameter for different realizations of the RLTL and report the sample average.

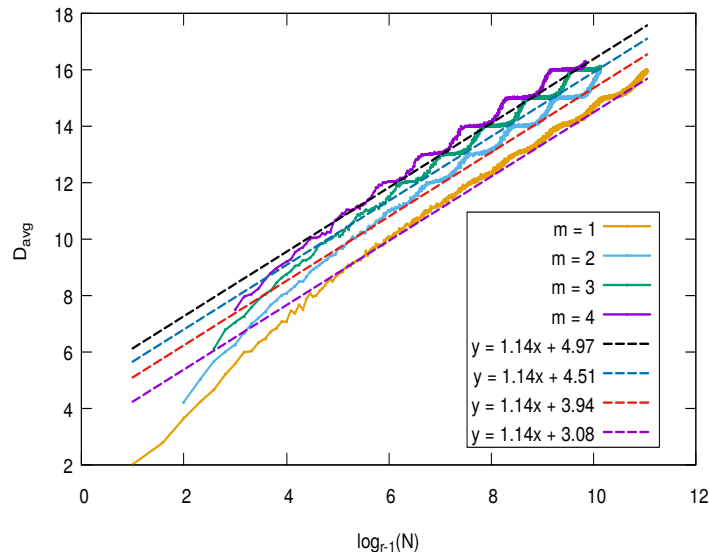


Figure 2.6: Sample-averaged diameter as a function of $\log_2(N)$. Each data point is sample-averaged over 100 independent realizations of the RLTL. The lower envelope of the curves have been fit to a straight line.

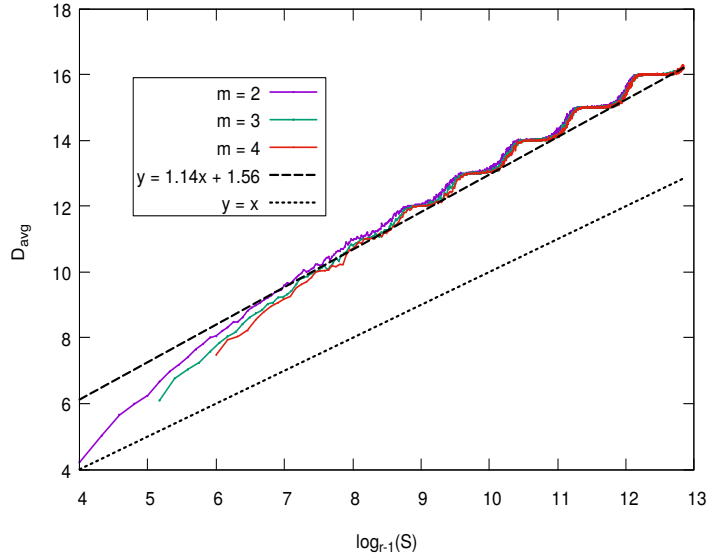


Figure 2.7: Sample-averaged diameter as a function of $\log_2(S)$. Each data point is sample-averaged over 100 independent realizations of the RLTL. The dashed line denotes the straight line used to fit the lower envelope of the curve. The dotted line gives the lower bound of $\log_{r-1}S$.

Figure 2.6 shows the sample-averaged diameter of the RLTL graphs as a function of the $\log_2(N)$ for different values of m . On plotting the diameter as a function of the logarithm of the total number of sites in the lattice (Fig. 2.7), we find that all these plots nearly collapse into a single curve. The lower envelope of this curve was fit to a straight line $y = 1.14\log_2(S) + 1.56$ (denoted by dashed line). The behavior of this lower envelope is consistent with the lower bound on the diameter given in Eq. 2.2, which we have shown using a dotted line.

We also check the upper bound on the diameter by plotting the sample-averaged diameter as a function of $x = \log_{r-1}(2.rS.\log(S))$ in Fig. 2.8. The dotted line shows the least integer satisfying Eq. 2.3 for $\varepsilon \sim 0$. The upper envelope of our diameter of the RLTL can be fit to a straight line of the form $y = x - 1.8$, which is consistent with the result of Bollobás.

A striking feature of all these plots is the stairway-like structure. This is not simply a consequence of the diameter being a discrete quantity. While the diameter of a lattice can take only integer values, the sample-averaged diameter can after all take values non-integer values. We can understand this feature by studying the sample-to-sample variation in the

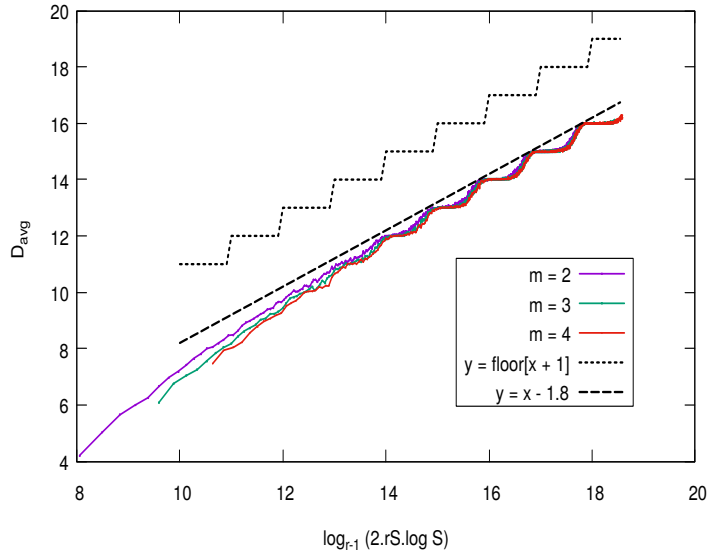


Figure 2.8: Sample-averaged diameter as a function of $\log_{r-1}(2.rS.\log(S))$. Each data point is sample-averaged over 100 independent realizations of the RLTL. The dashed line denotes the straight line used to fit the upper envelope of the curve. The dotted line gives the Bollobas upper bound in Eq. 2.3.

diameter for these lattices.

For different realizations of the RLTL with a given aspect ratio (m, N) , we look at the probability distribution of the diameters across samples. Fig. 2.9 shows this distribution for an RLTL with two bilayers for different values of N . We see that across different realizations of the RLTL with a fixed (m, N) , the distribution of the diameters is sharply peaked and is concentrated on at most 2-3 distinct values. We checked that this behavior was consistent for different number of bilayers. Almost all graphs of size S have a diameter that lies in $\{D - 1, D, D + 1\}$, where D is the integer closest to D_{avg} and is of $\mathcal{O}[\log_2 S]$. It turns out that the different realizations of the RLTL have nearly the same diameter.

In Fig. 2.10, we the plot of the sample-averaged diameter as a function of $\log(S)$ for an RLTL with $m = 4$ along with error bars that indicate the spread in the values of the diameter. From this figure, it becomes clearer that the step-like structure is a consequence of the low variation in the diameter across samples. In fact, we find the standard deviation in the diameter oscillates between 0 and 0.5 as shown in Fig. 2.11. The regions where the variance is close to zero corresponds to the flat regions in the plot of the diameter vs $\log(S)$.

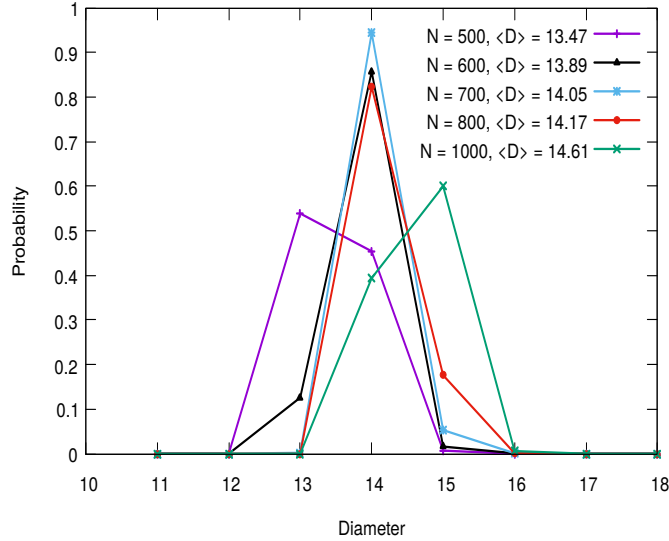


Figure 2.9: Probability distribution of the diameter of the RLTL across different realizations for $m = 2$ bilayers. For each N , the diameter was calculated for 1000 independent realizations of the RLTL. We observe that this distribution is sharply peaked and the diameter is concentrated around 2-3 values.

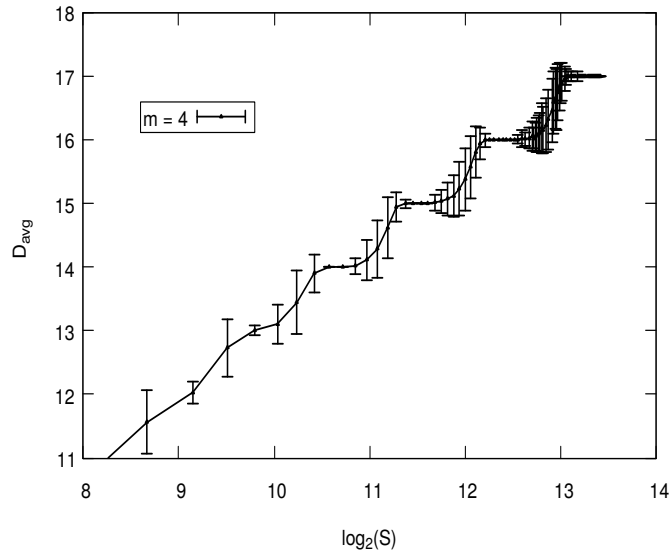


Figure 2.10: Sample-averaged diameter as a function of the logarithm of the total number of sites for an RLTL with $m = 4$ along with error bars. Each data point is averaged over 200 independent realizations of the RLTL. As seen, the step-like structure results from low variation in the diameter across different samples.

As an example, for $S \in [4880, 6000]$ where we observe a flat region in Fig. 2.10 at $D_{avg} = 16$, we found that the diameter was exactly 16 for 1000 independent realizations of the RLTL.

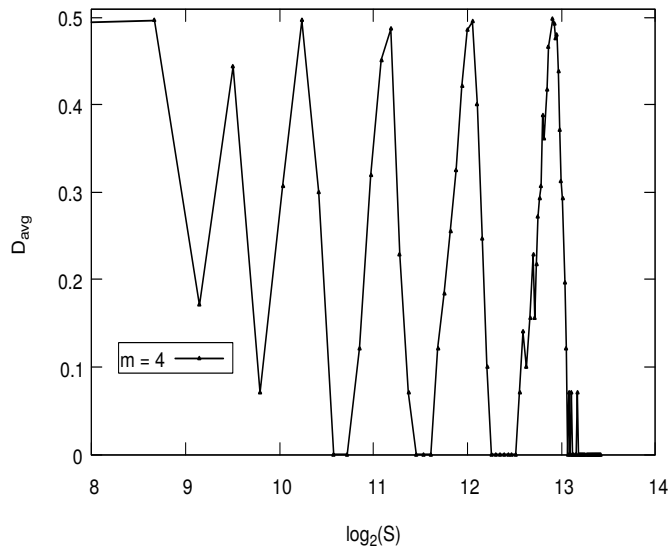


Figure 2.11: Sample-averaged standard error in the diameter as a function of the logarithm of the total number of sites for an RLTL with $m = 4$. Each data point is averaged over 200 independent realizations of the RLTL.

While the diameter takes only few distinct values across samples, we are also interested in how the distribution of the furthest distance from a site behaves within a lattice. We find that this (sample-averaged) probability distribution is also sharply peaked and is nearly the same for all sites. A representative plot for an RLTL with $m = 2$ is shown in Fig. 2.12.

Let us refer to the sites which have the maximum possible distance from them equal to the diameter as *extremal* sites. We now take a closer look and ask how these extremal sites are distributed across the lattice. If these extremal sites are closer together compared to the average distance between all sites in the lattice, that would give us a picture of the “shape” of the lattice. We plot the average distance between sites which have the *same* furthest distance possible in Fig. 2.13. We observe that these extremal sites are on an average spaced further apart from each other than the rest of the sites and are not clustered together. As an example, for $S = 200$, we observe that the maximum possible diameter of an RLTL is 13, while the sample-averaged diameter was 10.8. In this case, the typical number of

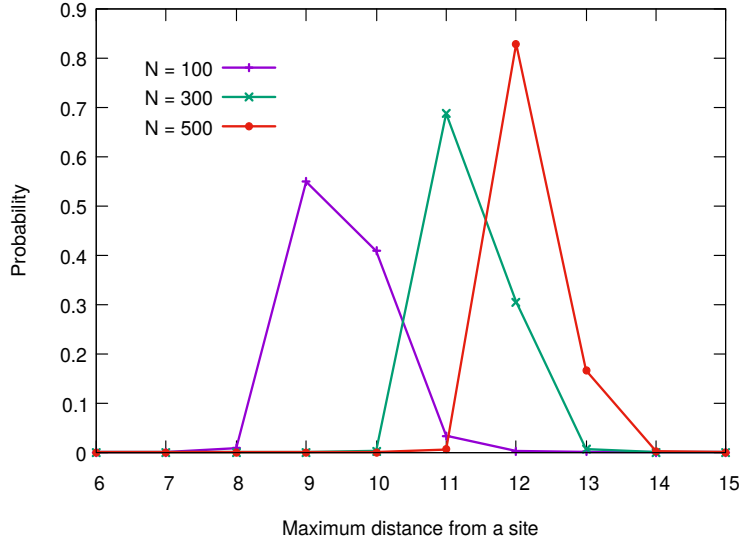


Figure 2.12: Probability distribution of the furthest distance possible from a site for an RLTL with two bilayers. The data is averaged over 1000 realizations of the RLTL for each N . We observe that for most sites, the farthest distance one can go is nearly the same value, different from the median by at most one.

extremal sites (with maximum possible distance equal to 13) was 5 and the average distance between two extremal sites is 8.2.

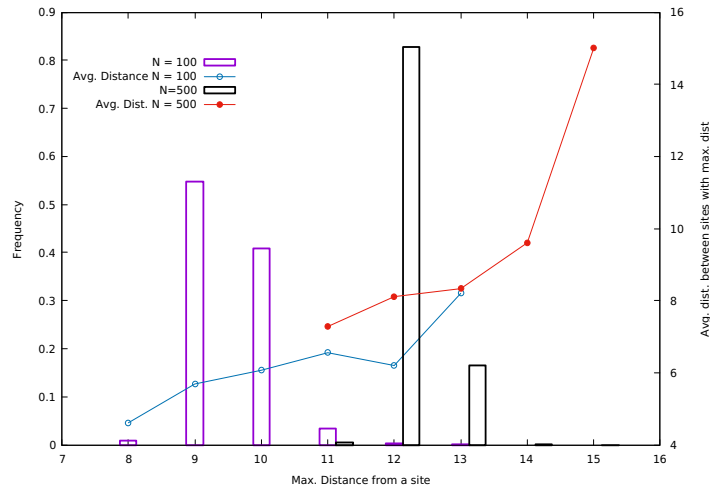


Figure 2.13: Studying the clustering of sites as a function of the furthest distance possible from it. Left Y axis: Probability distribution of the maximum distance possible from a site. Right Y axis: Probability distribution of the average distance between sites which have the same maximum distance. For each N , we average over 100 independent realizations of the RLTL with a single bilayer.

2.2 Radius of Gyration

The diameter of a graph is a measure of an extreme quantity and does not reflect the behaviour of majority of the sites in the graph. A more useful measure is provided by the radius of gyration which captures the behaviour of pairwise distances between all sites in the graph. For an arbitrary graph, we define this quantity as follows:

$$R_{gyr} = \sqrt{\frac{\sum_{u \in V, v \in V} (d(u, v))^2}{S}} \quad (2.4)$$

We numerically estimate the radius of gyration R_{gyr} of a realization of the RLTL by evaluating Eq. 2.4 by brute force. We start at a site (say a) and construct a breadth-first traversal tree around it. The tree terminates once all sites in the lattice are covered. A site b located at depth j in the tree thus has distance $d(a, b) = j$ from site a . At each step while building the tree, we add the squares of the distances between site a and the sites present at that particular depth. This is then repeated for all sites in the lattice to obtain the sum of the squares of the distances between all possible pairs of sites in the lattice.

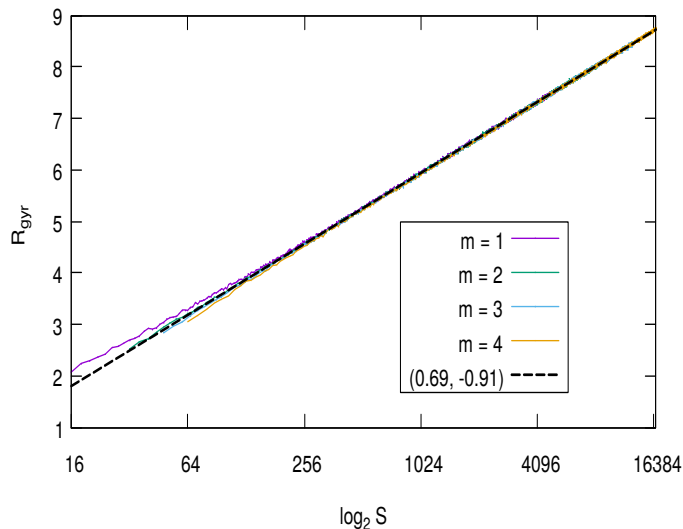


Figure 2.14: Sample-averaged radius of gyration (R_{gyr}) plotted as a function of the $\log(S)$ lattices upto 4 bilayers. Each data point is sample-averaged over 100 different realizations of the RLTL. The plots collapse for different values of m . The data is fit to a straight line; the ordered pair indicates the value of the slope and the intercept.

We calculated the sample-averaged radius of gyration using 100 independent realizations of the RLTL. We find that this quantity is also linear in the logarithm of the total number of sites in the lattice with the plots for different values of m all collapsing onto the same curve as shown in Fig. 2.14.

2.3 Study of sites at distance r from a point

Suppose we pick any site on the RLTL and study the number of distinct neighbours present at a distance r from it. Upto a distance $\mathcal{O}[\log N]$ where locally tree-like approximation is valid, this would follow the curve 3.2^{r-1} . Beyond this, we expect deviations due to the presence of loops. This behaviour was seen in Fig. 2.5, where we looked at the average number of distinct sites present at distance r from a site. Thus, this quantity gives us insight into presence of short loops on the lattice, particularly the length at which they arise and how many there are. How does the distribution of these short loops vary across sites in the lattice? Are there sites which are part of more short loops compared to the others? To study this further, we define a quantity $g(r)$ as the average fractional number of distinct sites present *within* the shell of radius r surrounding a site. Sites that have more number of short loops passing through them would have a lower value of $g(r)$ than average (where r is lesser than the diameter).

In particular, we study the fraction of sites present in the r^{th} shell averaged over extremal sites and compare it to fraction of sites present in the r^{th} shell averaged over all sites. The resulting plot is shown in Fig. 2.15 for a lattice with a single bilayer and $N = 500$. To better visualize the difference, we plot the ratio of average fraction of sites present within the r^{th} shell for all sites to that of the extremal sites as a function of r in Fig. 2.16. These results indicate that there are more number of short loops passing through extremal sites than average (and hence there are fewer distinct sites at a distance r from them than average). This result is in hindsight not surprising — due to the presence of more number of short loops, one has to go deeper in a breadth-first traversal tree constructed around such sites in order to visit all sites in the lattice. In other words, the presence of more number of short loops is what makes these sites extremal. We observe that for fixed S , this effect is more pronounced for small m .

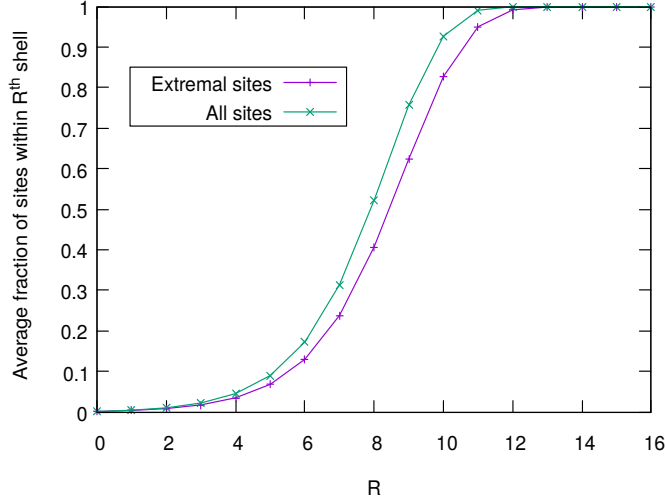


Figure 2.15: Fraction of sites within the r^{th} shell averaged over extremal sites compared to the average over all sites in the lattice. Each data point is sample-averaged over 100 realizations of the RLTL with $m = 1$ and $N = 500$.

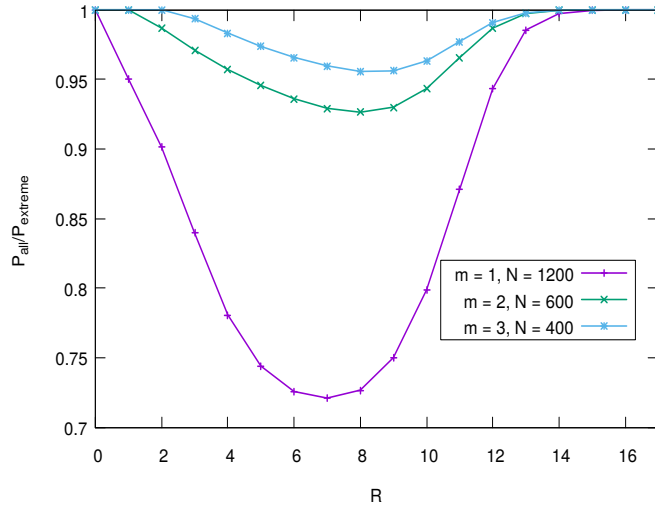


Figure 2.16: Ratio of the fraction of sites within the r^{th} shell surrounding a point averaged over all sites (P_{all}) to that of extremal sites ($P_{extremal}$) as a function of r for a fixed value of $S = 2400$. Each data point is sample-averaged over 100 realizations of the RLTL.

Probability distribution of distances between sites

A consequence of the presence of the interlayer permutation bonds in the RLTL is that the spatial distribution of sites present in the r^{th} shell surrounding a site in the lattice is nearly

random. For large N , if we pick a site on the RLTL and study the sites in the r^{th} shell, we expect them to be roughly randomly distributed on the lattice. This motivates us to think in terms of the combinatorial problem of choosing balls at random and coloring them.

Suppose we have S balls in total. We first pick n_1 balls at random and color them red. Next, we independently (after replacement of the n_1 balls) pick n_2 balls at random and color them green. The probability that a ball does not get colored *both* red and green is then:

$$P(\bar{R} \cap \bar{G}) = \frac{\binom{S}{n_1+n_2}}{\binom{S}{n_1} \binom{S}{n_2}}$$

where \bar{R} and \bar{G} denotes the event of a ball not being colored red or green respectively.

If n_1/S and $n_2/S \ll 1$, then this can be approximated as follows:

$$P(\bar{R} \cap \bar{G}) = \exp\left[-\frac{n_1 \cdot n_2}{S}\right]$$

We can now apply this result to the RLTL. Suppose we pick two random points O_1 and O_2 on the RLTL, and we study the sites present within shells of radius R_1 and $R_2 = \log_2 S/2$ around these points. Using the locally tree-like property, we know the number of sites within the shells is $n_1 = 3 \cdot 2^{R_1} - 2$ and $n_2 = 3 \cdot 2^{R_2} - 2$ respectively. As discussed previously, for large N , these sites are *approximately* randomly distributed on the lattice. We introduce a factor α to account for the fact that these sites are not truly randomly distributed due to the non-permutating (zig-zag) bonds. We expect α to be of $\mathcal{O}(1)$.

Let us color the n_1 sites in the shell surrounding point O_1 red and the n_2 sites in the shell surrounding point O_2 green. The probability that a site in the lattice does not get colored either green or red is the same as the probability that the distance between O_1 and O_2 is greater than $R_1 + R_2$:

$$P[d(O_1, O_2) \geq R_1 + R_2] = \exp\left[\frac{n_1 \cdot n_2}{\alpha S}\right]$$

where we expect α to be a constant of $\mathcal{O}(1)$. Substituting the values of n_1 and n_2 under the locally tree-like approximation, we get:

$$P(d(O_1, O_2) \geq R_1 + R_2) = \exp\left[-\frac{9 \cdot 2^{R_1+R_2}}{4 \alpha S}\right] \quad (2.5)$$

Numerically verifying this result: For each site in the RLTL, we find the fraction of sites in the lattice located on the R^{th} shell surrounding it. We repeat this for all the sites in the lattice to obtain the average fraction of sites located at distance R from a site. This is then sample-averaged over different realizations of the RLTL. Using this data, we can calculate the probability that the distance between two sites is greater or equal than R .

For simplicity, we consider an RLTL with a single bilayer and plot this probability as a function of R for different values of N as shown in Fig. 2.17. Absorbing all the constants into a single constant a (which is independent of N but depends on m), we can write Eq. 2.3 as:

$$P(d(u, v) \geq R) = \exp \left[-\frac{2^R}{aN} \right] \quad (2.6)$$

The probability distribution we obtain numerically is shown in Fig. 2.17.

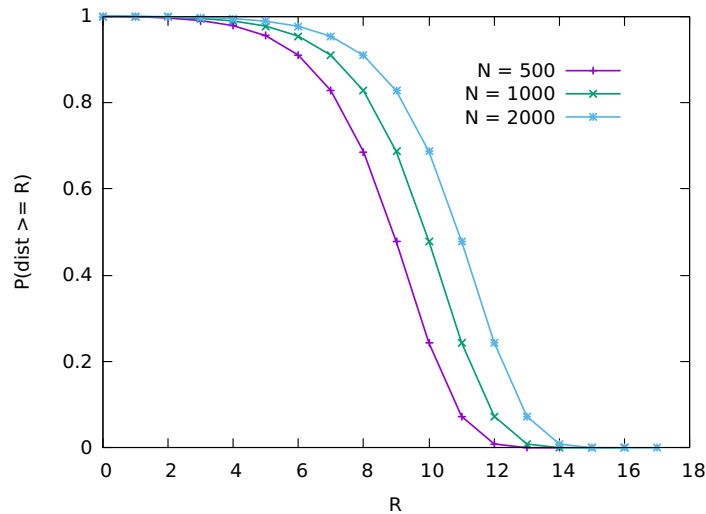


Figure 2.17: Sample-averaged probability that the distance between two randomly picked sites is greater at R as a function for R for the RLTL with a single bilayer $m = 1$. Each data point is averaged over 100 independent realizations of the RLTL.

To find the value of a and check that it is indeed independent of N , we plot the logarithm of the probability $P(R)$ as shown in Fig. 2.18. We then try to fit these curves to a function of the following form (taking the logarithm of Eq. 4).

$$\log(P(R)) = -\frac{2^R}{aN} \quad (2.7)$$

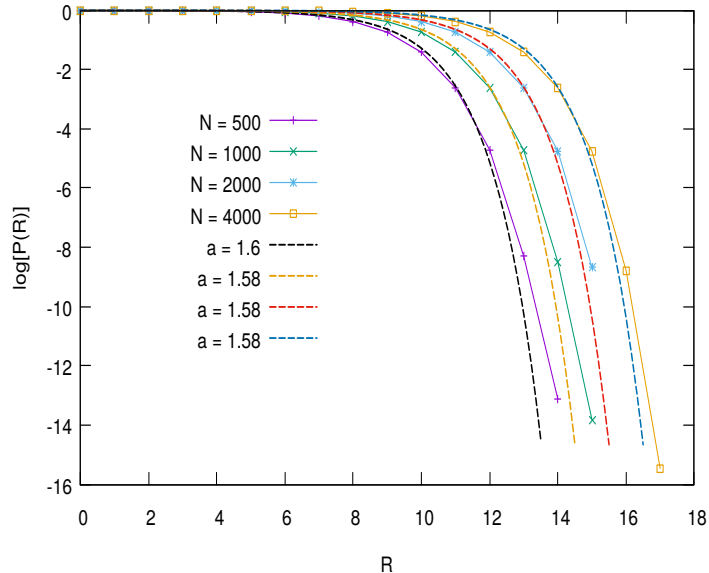


Figure 2.18: Logarithm of the probability that two randomly chosen sites on the RLTL are at a distance greater than R from each other as a function of R for lattices with a single bilayer. The curves are then fitted to the form given in Eq.2.7. We find that value of a to be ~ 1.58 .

Since this result is valid within the locally tree-like region, we fit the function to the initial data points and ignore deviations at $R \geq \log_2 N$. We find that we are able to obtain a value of $a \sim 1.58$ consistent with these equations and our order of magnitude expectation.

2.4 Four coordinated RLTL

While we have discussed three-coordinated graphs, most of the results are easily extended to graphs of higher coordination numbers. We can define an RLTL with coordination number four on similar lines as the three-coordinated RLTL. The broad idea behind the construction of one realization of four-coordinated RLTL is to take independent bilayers connected via zig-zag bonds and construct zig-zag bonds between the bilayers *after* randomly permuting the indices of sites. We explicitly describe this construction in this section. This lattice is built out of *layers* and we denote the number of layers by m . Let the number of sites in

each layer be N . Then the total number of sites in the lattice is $S = m * N$. We label sites in each layer by integers 1 to N .

1. Between layer 1 and layer 2, we form zig-zag bonds as usual. Site i in layer 1 is connected to site i and $(i + 1)$ in layer 2. Periodic boundary conditions are imposed in the lateral direction so that site N in layer 1 links to site 0 in layer 2. We do not need to permute the labels of sites in layer 1 as these are arbitrary to begin with.
2. The labels of sites in layer 2 are now permuted. Let us call this permutation σ_2 . We then form zig-zag bonds between the *relabelled* sites of layer 2 and sites in layer 3 (which are labelled as usual). To state it explicitly: site k in layer 2 is connected to sites $\sigma_2(k)$ and $\sigma_2(k) + 1$ in layer 3 (with appropriate periodic boundary conditions).
3. Now we relabel sites in layer 3 by a random permutation and form zig-zag bonds between layer 3 and 4 on same lines described in step 2. We repeat this procedure for all layers.
4. We impose periodic boundary conditions in the transverse direction. So the last layer m is connected back to layer 1. To avoid too many loops of size four, we permute the labels of sites in layer 1 as well.

The first two steps of this process are shown in Fig. 2.19. We only consider lattices with even m so that the graph is bipartite.

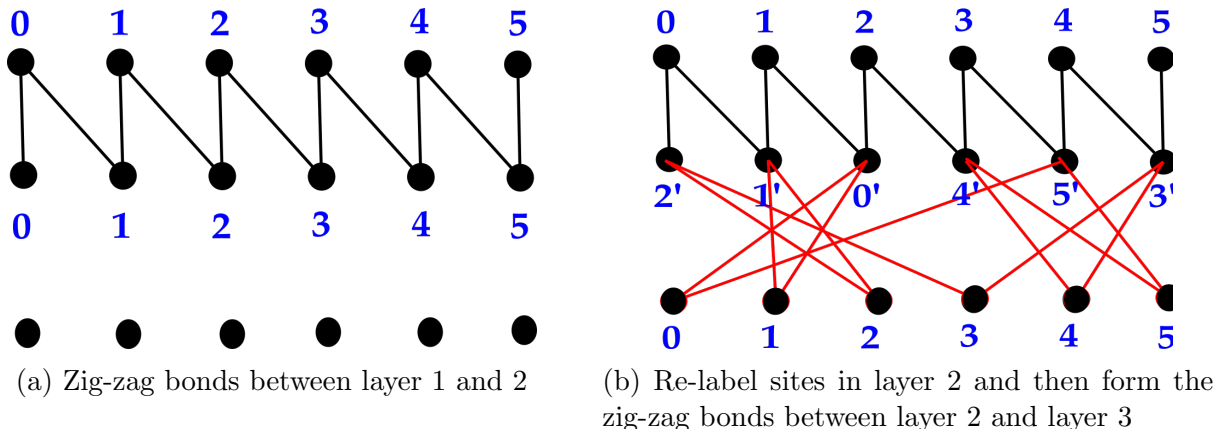


Figure 2.19: Constructing the 4-coordinated RLTL (shown: the first two steps without the boundary conditions).

2.4.1 Diameter

As a verification that our previous results on the study of the diameter of the three-coordinated RLTL hold on this lattice as well, we plot the sample-averaged diameter as a function of $x = \log_{r-1}(2.rS.\log(S))$ for the four-coordinated ($r = 4$) lattice as well. We see in Fig. 2.20 that the plots for different m collapse onto a single curve. The diameter of the order of the logarithm of the total number of sites and shows the step-like structure.

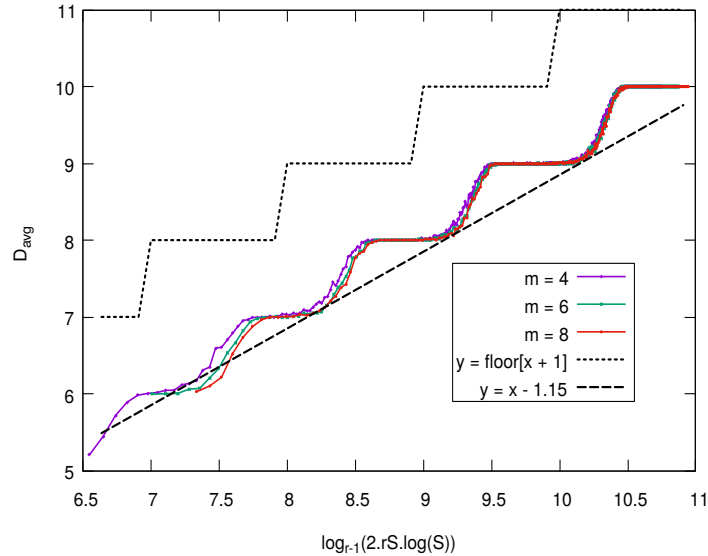


Figure 2.20: Sample-averaged diameter as a function of $x = \log_{r-1}(2.rS.\log(S))$ for the four-coordinated RLTL where $r = 4$. Each data point is averaged over 200 independent realizations of the RLTL. The dotted line denotes the bound given by Bollobas in Eq. 2.3

2.5 Shortest loop passing through a point

The presence of loops on the RLTL makes the behaviour of various quantities deviate from what is expected on the Bethe lattice. Hence, it is important to take a closer look at the shortest loop passing through any given point. Note that this is slightly different from our discussion in section 2.0.1, where we just looked at the probability that a site has a loop of size l . Here we look at what fraction of sites have the length of *shortest* loop passing through

them equal to l .

Numerically studying the shortest loop passing through a point: To find the shortest loop passing through a site A , we begin by constructing a breadth-first traversal tree around the site. If at depth d , we reach a site which is already part of this tree, we have found a loop. Site A however, might not be a part of this loop. We then traverse this loop to check whether site A is indeed part of it or not. If it is, the length of the shortest loop passing through A is $2d$.

We first look at how this distribution changes as we vary the number of sites per layer N for lattices with fixed number of layers. This is shown for the three and four coordinated RLTL with $m = 4$ in Fig. 2.21. We see that the length of the shortest loop through a site on the three-coordinated RLTL (Fig. 2.21a) is on average longer than that on the four-coordinated RLTL (Fig. 2.21b). This is expected as the additional inter-layer bonds increases the probability of having loops of shorter sizes. We also see that as the number of sites in each layer is increased, the distribution shifts towards the right — i.e., the length of the most probable shortest loop increases.

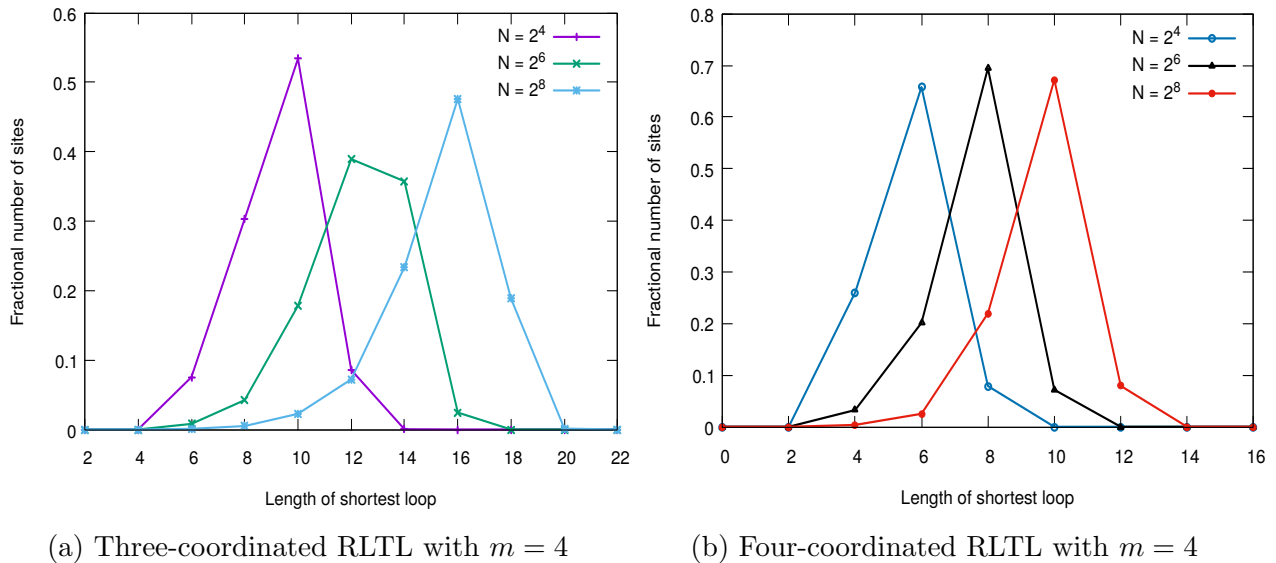
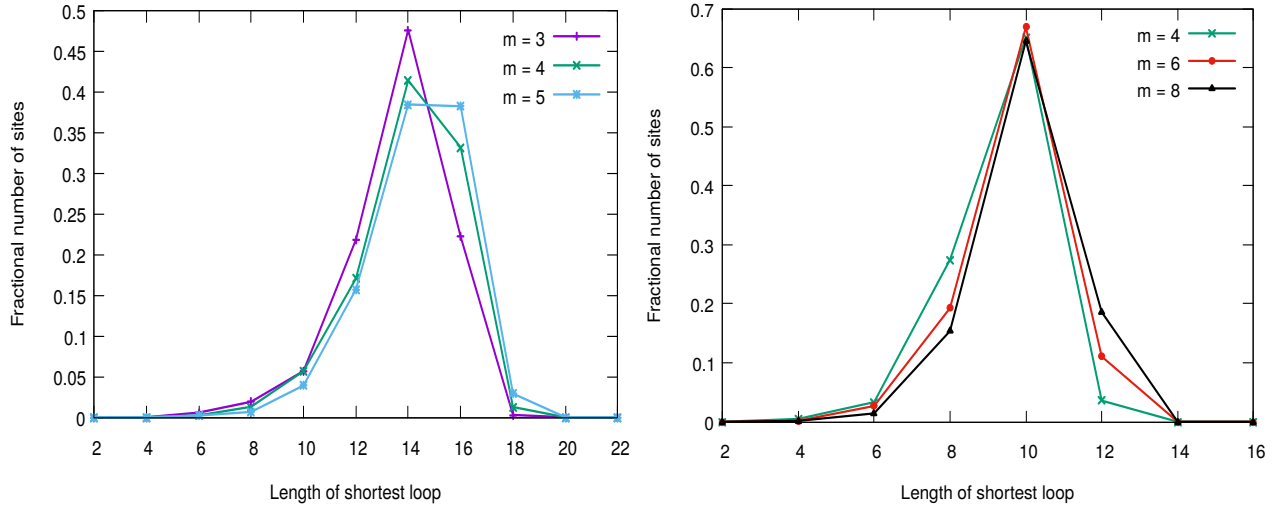


Figure 2.21: Distribution of the size of the average shortest loop passing through a site on RLTLs with fixed M . Each data point is sample-averaged over 100 independent realizations.

For lattices with fixed N , we see that the effect of increasing the number of layers is not as substantial (see Fig. 2.22). The length of the most probable shortest loop passing through a site does not change much but the fraction of sites having shortest loops of very



(a) Three-coordinated RLTL with $N = 2500$

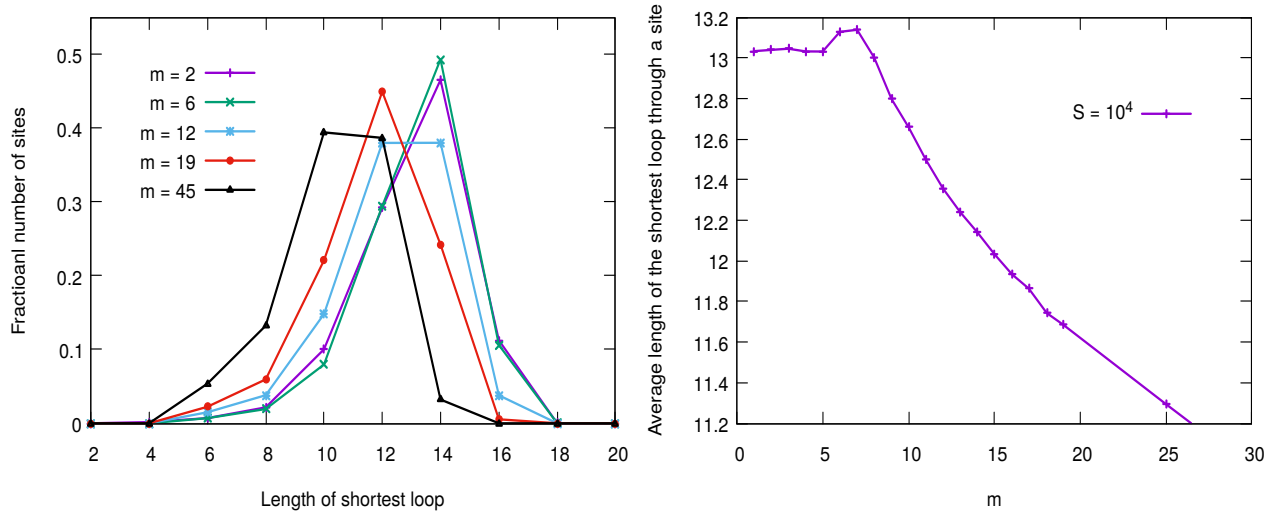
(b) Four-coordinated RLTL with $N = 5000$

Figure 2.22: Distribution of the size of the average shortest loop passing through a site on the RLTL for fixed N . Each data point is sample-averaged over 100 independent realizations.

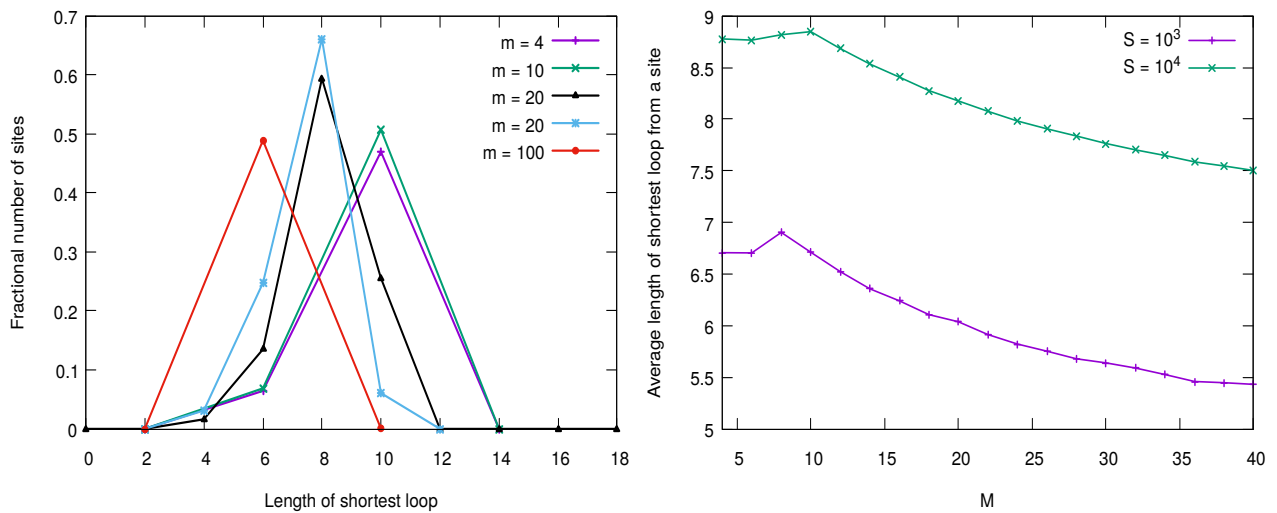
small length does decreases.

To understand the role of the aspect ratio in the distribution of the shortest loop passing through a site, we look at this distribution for lattices with fixed number of sites S but different number of layers. Fig. 2.23 summarizes our results from this study. We observe that for lattices with more number of layers, the distribution shifts to the left —implying that there are more number of shorter loops passing through a site. The size of the average shortest loop passing through a site reduces, as seen in Fig. 2.23b and 2.23d.

Our data suggests that for a fixed (and finite) S , lattices with smaller number of layers have longer shortest loops passing through the sites. This is contrary to what one would naively expect. For a lattice with small number of layers ($m \gg N$), one would assume that the shortest loop passing through a site would be a very short loop (of order m) that “wraps” around the lattice in the transverse direction and shifts the distribution to the left. However, we see that such order m loops are actually unlikely. The shortest loop passing through a site on an RLTL with small number of layers may still wrap around the lattice but ends up being a longer than a simple loop of order m . This leads us to another line of study of the “winding” number of loops.



(a) Distribution of the shortest loop passing through a point for lattices with fixed $S = 10^4$ and different aspect ratios (m, N). (b) Average length of the shortest loop passing through a point as a function of m



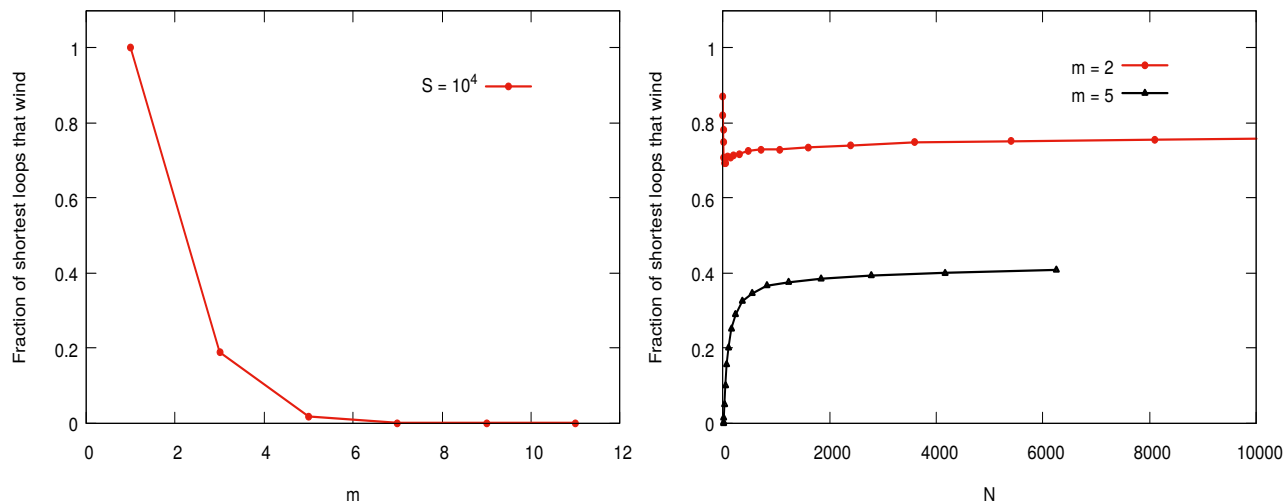
(c) Distribution of the shortest loop passing through a point for lattices with fixed $S = 10^4$ and different aspect ratios (m, N). (d) Average length of the shortest loop passing through a point as a function of m

Figure 2.23: Understanding the effects of the aspect ratio of the RLTL: study of the distribution of the shortest loop passing through a site for the three-coordinated (top panel) and four-coordinated RLTL (bottom panel) for a fixed number of total sites (S). Each data point is sample-averaged over 100 independent realizations.

2.5.1 Winding loops

The RLTL of a given total number of sites S is actually an ensemble of lattices with different values (m, N) . When studying different models in statistical physics on this lattice — especially when characterizing finite-size effects — it is important to reduce the anisotropy present in the lattice. Thus, while studying the shortest loop passing through a point, we are interested in what fraction of these loops wind in the transverse direction. One way of achieving this is to have the fraction of loops winding around the lattice in the transverse direction to be close to 0.5.

We numerically study this on the RLTL. It is straightforward to find a winding number of a given loop: Once we have a list of sites that form a loop (with the order specified: say $\{a, b, c, \dots, a\}$), we simply traverse the loop and have a counter that keeps tracks of the increase (or decrease) in the layer number of the sites in the loop. The winding number of a given loop is then the absolute value of this counter modulo the number of layers in the lattice.

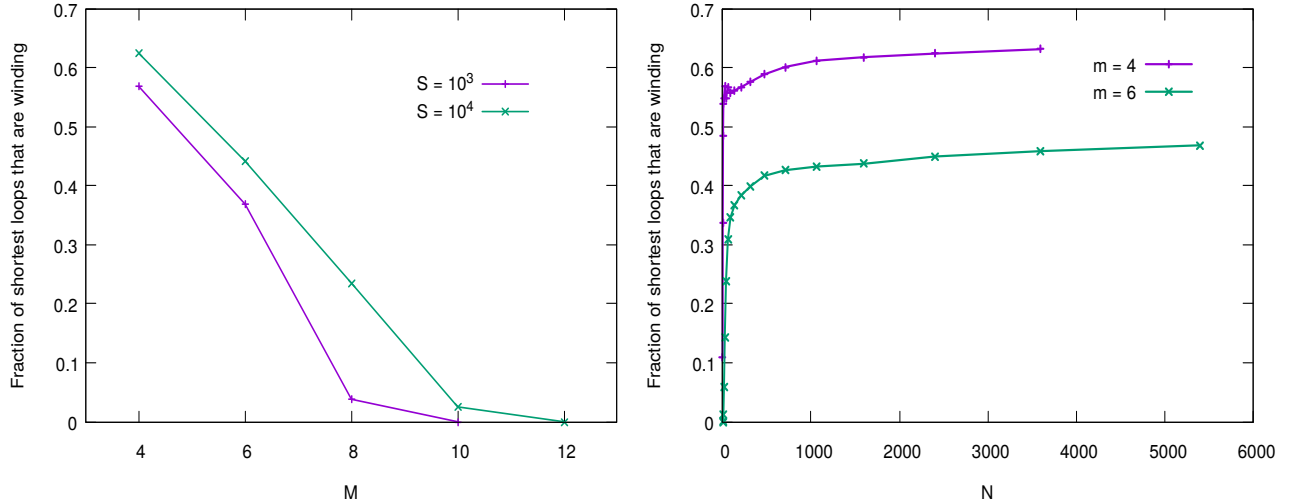


(a) Fraction of short loops that wind around the lattice as a function of m for fixed S .

(b) Fraction of short loops that wind around the lattice as a function of N for fixed m .

Figure 2.24: Understanding the effects of the aspect ratio of the RLTL: study of the fraction of shortest loops passing through a site that wind around the three-coordinated RLTL in the transverse (m) direction. Each data point is sample-averaged over 100 independent realizations of the RLTL.

Figs. 2.24 and 2.25 shows the plot of the fraction of shortest loops that wind around the



(a) Fraction of short loops that wind around the lattice as a function of m for fixed S .

(b) Fraction of short loops that wind around the lattice as a function of N for fixed m .

Figure 2.25: Understanding the effects of the aspect ratio of the RLTL: study of the fraction of shortest loops passing through a site that wind around the four-coordinated RLTL in the transverse (m) direction. Each data point is sample-averaged over 100 independent realizations of the RLTL.

lattice for fixed S and fixed M respectively. As expected, for a fixed total number of sites, this fraction tends to zero for lattices with larger number of layers. For lattices with small number of layers, most of loops are winding. In fact, for the three-coordinated RLTL with a single bilayer, although it is in principle possible to have loops which do not wind around the lattice, we found that almost all loops are winding for $S = 10^4$.

Returning to our original idea of reducing the anisotropy in the lattice: For lattices with a given number of layers, we try to find a value of N at which this fraction would be approximately half so that a short loop is equally like to wind around the transverse direction or not wind. We see in Fig. 2.25b that for four-coordinated lattices with number of layers $m > 6$ and three-coordinated lattices with number of bilayers $m > 5$, the fraction of winding loops grows slowly in N . So the shortest loop in the lattice, even for $m \ll N$ do not all wrap around the lattice in the transverse direction.

Chapter 3

The Ising Model on the RLTL

This chapter contains a detailed study of the Ising model on the RLTL. In the limit of large number of sites, the behaviour of the Ising model on the RLTL is exactly the same as the Bethe lattice — i.e., the free energy per site for the RLTL $f_N(T)$ coincides with the result on the Bethe lattice $f_{Bethe}(T)$. However, for a finite number of sites, there will be deviations from what is expected in the thermodynamic limit. We quantify these deviations by studying the finite-size scaling on this lattice. First, we recapitulate the explicit expressions for the behaviour of the Ising model on the Bethe lattice. Next, we perform Monte-Carlo simulations of the Ising model on the RLTL and summarize the results of our studies. Finally, we discuss the finite-size scaling of the specific heat capacity and magnetic susceptibility on this lattice.

We study the Ising model with nearest-neighbour interactions, which has the following Hamiltonian:

$$E(\sigma) = -J \sum_{\langle i,j \rangle} \sigma_i \sigma_j - H \sum_i \sigma_i$$

Here $\langle i, j \rangle$ indicates a sum over all the nearest-neighbour pairs of spins in the lattice, J is the strength of the coupling between spins and H is the external magnetic field.

The partition function for the system can then be written as:

$$Z_N = \sum_{\sigma} \exp \left(K \sum_{\langle i,j \rangle} \sigma_i \sigma_j + h \sum_i \sigma_i \right) \quad (3.1)$$

where $K = J/k_B T$ and $h = H/k_B T$.

Let us consider the case of no external magnetic field ($H = 0$). We will derive equations for the behaviour of this zero-field Ising model on the three-coordinated Bethe lattice. The arguments presented here are on similar lines to the treatment given in Baxter's book (Ref. [6]).

3.1 Ising model on the Bethe lattice

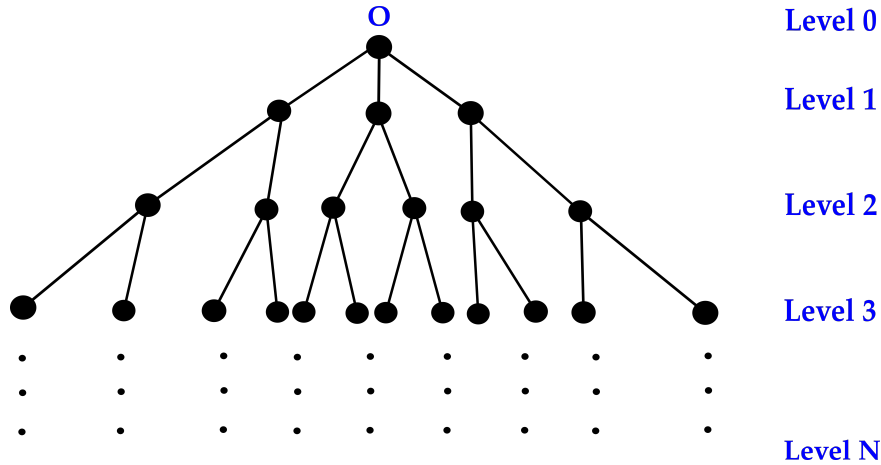


Figure 3.1: A three-coordinated Cayley tree consisting of N levels centred at site O .

To obtain the behaviour of the Ising model on the Bethe lattice, we look at the Ising model on the Cayley tree and only consider the effect of sites *deep within* the graph — i.e., we effectively ignore the contribution that the sites at the boundary make to the partition function.

Suppose we have a Cayley tree consisting of N levels centred at site O as shown in Fig. 3.1. We pick an arbitrary site a at level r in the tree. Since the graph is three-coordinated, this site is connected to two sites b and c in the subsequent level $r + 1$. Sites b and c form

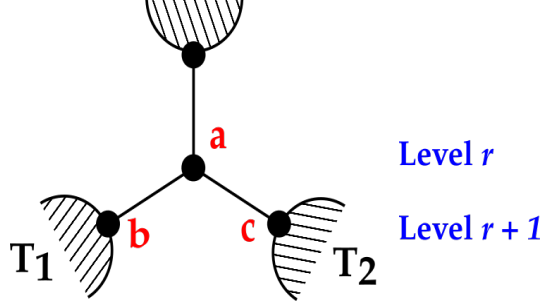


Figure 3.2: Site a at level r in the Cayley tree connected to two subtrees T_1 and T_2 below via sites b and c at level $r + 1$.

the root of two sub-trees T_1 and T_2 which are connected to a as shown in Fig. 3.2. Let us define $Z_T(\sigma_i)$ to be the restricted partition function of a given branch T keeping the spin at the root of the branch (σ_i) fixed. The restricted partition function at site a due to the sites “below” it can then be expressed in terms of the restricted partition functions of the sub-trees T_1 and T_2 as:

$$Z(\sigma_a) = \sum_{\sigma_b, \sigma_c} e^{\beta J(\sigma_a \sigma_b + \sigma_a \sigma_c)} Z_{T_1}(\sigma_b) Z_{T_2}(\sigma_c) \quad (3.2)$$

where $\beta = \frac{1}{k_B T}$

Consider the sub-tree rooted at a site b . We can express the effect of the sites in the levels beyond b by an effective field H_1 at site b . The restricted partition function at the sub-tree rooted at b can then be written as $Z_{T_1}(\sigma_b) = K_b e^{\beta H_1 \sigma_b}$. Similarly, the restricted partition function of the sub-tree rooted at site c can be expressed in terms of the effective field H_2 as $Z_{T_2}(\sigma_c) = K_c e^{\beta H_2 \sigma_c}$.

Each partition functions appearing in Eq. 3.2 can be expressed in the form $Z(\sigma_i) = K^i (1 + h_i \sigma_i)$, where $h_i = \tanh \beta H_i$. Using this form, and then integrating out the spins σ_b and σ_c , the effective field at σ_a (due to the rest of the lattice in the levels beyond it) turns out to be:

$$\tilde{h} = \frac{x_0(h_1 + h_2)}{1 + x_0^2 h_1 h_2} \quad (3.3)$$

where $x_0 = \tanh \beta J$

The left hand side of Eq. 3.2 is simply the restricted partition of the sub-tree at level r rooted at site a . So, we can keep repeating the above process at each level in the tree and integrate inwards to get the effective field at a site (due to the sites beyond it) in the previous level. In other words, Eq. 3.3 can be applied recursively at each level. As noted before, we are interested in the behaviour of the sites *deep within the lattice*. Presumably if we look deep inside the lattice, this effective field would be independent of the level that the site is in. In other words, we are interested in the fixed point of Eq. 3.3. This fixed point, which we call $h^*(= \tanh\beta H^*)$, depends on the value of x_0 .

$$h^* = \frac{2x_0 h^*}{1 + x_0^2 h^{*2}} \quad (3.4)$$

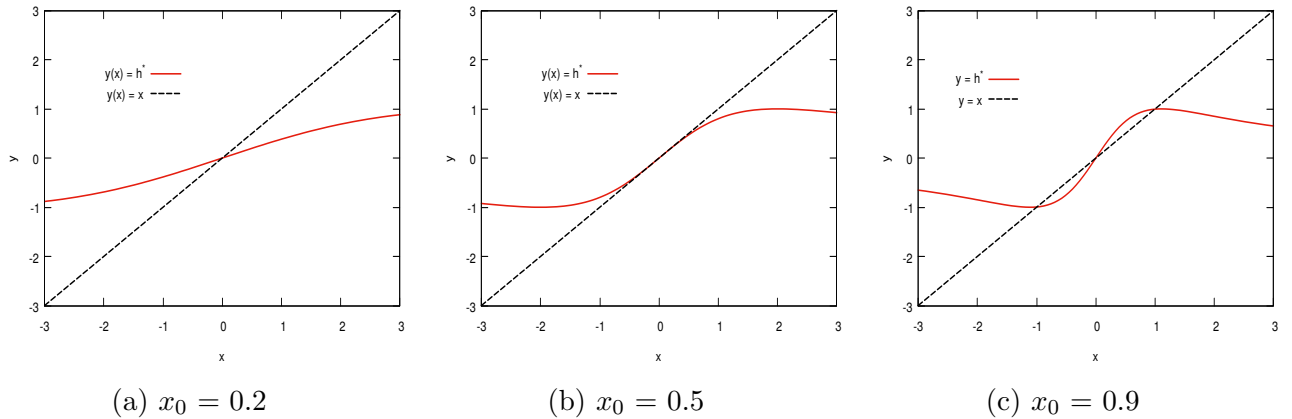


Figure 3.3: Solutions to the recursion equation Eq. 3.3 for different values of x_0 . Note that the range of x_0 is $[-1,1]$.

Fig. 3.3 illustrates the how this fixed point change with x_0 . If $x_0 < \frac{1}{2}$, the effective field at each level keeps decreasing as we move inward away from the boundary of the Cayley tree and eventually goes to zero.

If $x_0 > \frac{1}{2}$, Eq. 3.3 has three fixed points, two of which are stable points. The effective field tends to either one of these stable points $h^* = \pm \sqrt{\frac{2x_0-1}{x_0^2}}$ depending on the boundary conditions.

Thus, there is a critical value of $x_0 = \frac{1}{2}$ at which the behavior of the effective field changes. This corresponds to a $T_c = \frac{2J}{k_B \ln 3}$. In general, for a Bethe lattice with coordination number q , the critical point is:

$$\frac{J}{k_B T_c} = K_c = \frac{1}{2} \ln \left[\frac{q}{q-2} \right] \quad (3.5)$$

To get the full field at a site, we need to consider the effect of all the three sub-trees connected to it. Consider any site deep within the Cayley tree with a spin σ_0 . The three sub-trees connected to σ_0 are independent of each other. We already know that deep within the lattice, the effective field at a site due to the sites below it in the tree is H^* given by Eq. 3.4. The full field at the spin σ_0 can be expressed in terms of H^* using the picture provided in Fig. 3.4.

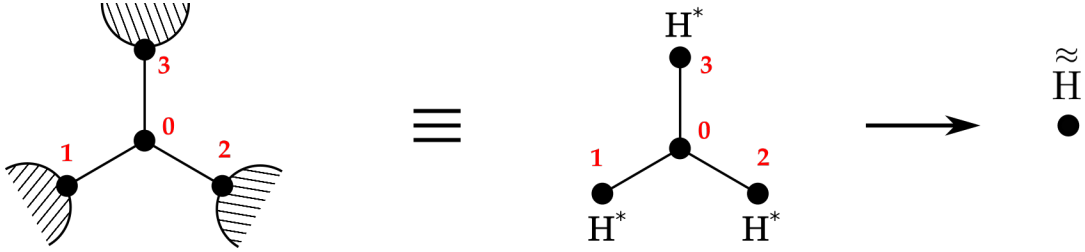


Figure 3.4: Effective field at a site on the Bethe lattice

The full partition function at spin σ_0 can be written as:

$$\begin{aligned}
Z_0(\sigma_0) &= \sum_{\sigma_1, \sigma_2, \sigma_3} e^{\beta J \sigma_0 (\sigma_1 + \sigma_2 + \sigma_3)} Z_{eff}(\sigma_1) Z_{eff}(\sigma_2) Z_{eff}(\sigma_3) \\
&\propto \sum_{\sigma_1, \sigma_2, \sigma_3} (1 + x_0 \sigma_2 \sigma_0) (1 + x_0 \sigma_3 \sigma_0) (1 + x_0 \sigma_1 \sigma_0) (1 + h^* \sigma_1) (1 + h^* \sigma_2) (1 + h^* \sigma_3) \\
&\propto (1 + h^* x_0 \sigma_0)^3
\end{aligned}$$

Expressing the partition function at σ_0 as $Z_0(\sigma_0) \equiv A(1 + \tilde{h}\sigma_0)$, we obtain an equation for the full field \tilde{h} at a site as:

$$\tilde{h} = \frac{3x_0 h^* + x_0^3 h^{*3}}{1 + 3x_0^2 h^{*2}} \quad (3.6)$$

3.1.1 Magnetization per site (m)

In the absence of any external magnetic field, the magnetization per site is simply:

$$m_s(T) = \frac{3x_0 h^* + x_0^3 h^{*3}}{1 + 3x_0^2 h^{*2}}$$

Using the expressions for h^* , this gives us:

$$m_s(T) = \begin{cases} 0 & T > T_C \\ \pm \left(\frac{2x_0-1}{x_0^2} \right)^{1/2} \frac{3x_0+x_0^3 \left(\frac{2x_0-1}{x_0^2} \right)^2}{3(2x_0-1)+1} & T \leq T_C \end{cases} \quad (3.7)$$

3.1.2 Energy per site (e)

The energy *per bond* can be expressed in terms of the effective field due to two sub-trees as shown in Fig. 3.5:

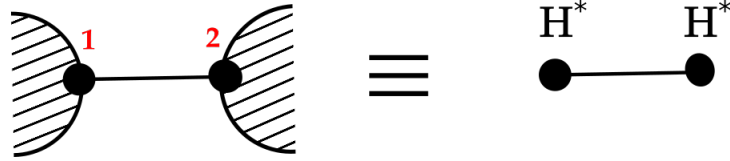


Figure 3.5: Calculation of the energy per bond using the effective field due to the sub-trees.

$$\begin{aligned} E_b(T) &= -J \langle \sigma_1 \sigma_2 \rangle \\ &= -J \sum_{\sigma_1, \sigma_2} \frac{\sigma_1 \sigma_2 P(\sigma_1, \sigma_2)}{Z} \\ &= -J \frac{x_0 + h^{*2}}{1 + x_0 h^{*2}} \end{aligned}$$

Since each site is connected to three neighbours via bonds that are shared between two sites, the energy per site is 3/2 the energy per bond. Substituting the expression for h^* , the energy per site is then:

$$e_s(T) = \begin{cases} -\frac{3J}{2} x_0 & T > T_C \\ -\frac{3J}{2} \frac{(x_0^3+2x_0-1)}{x_0(3x_0-1)} & T \leq T_C \end{cases} \quad (3.8)$$

3.1.3 Specific Heat Capacity (C_v)

The specific heat capacity is defined as $C_v = \frac{dE}{dT}$. For simplicity, we set both J and k_b to 1. This gives us the following expressions for the specific heat capacity per site:

$$C_v(T) = \begin{cases} \frac{1.5}{(T \cosh(\frac{1}{T}))^2} & T \geq T_C \\ \frac{2.25 - 0.75 \exp(-4/T) - 3 \exp(-2/T)}{(\sinh(1/T))^4 (\cosh(1/T))^2 x_0^2 (3 - \coth(1/T))^2} & T < T_C \end{cases} \quad (3.9)$$

The specific heat on the Bethe lattice shows a finite jump at the critical temperature.

3.1.4 Magnetic Susceptibility (χ)

The magnetic susceptibility is defined as:

$$\chi = \lim_{H \rightarrow 0} \frac{dM}{dH}$$

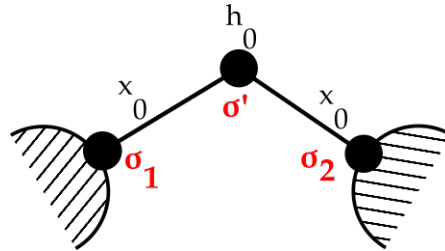


Figure 3.6: Site σ' at a level r in the tree

To calculate the susceptibility, we first need to find the magnetization in the presence of a small external field. Let us introduce a small external field $h_0 = H/kT$. The restricted partition function for a spin σ' at level r in the Cayley tree due to the sub-trees at level $r+1$ below it can be written as:

$$Z_r(\sigma') = \sum_{\sigma_1, \sigma_2} Z_{r+1}(\sigma_1) Z_{r+1}(\sigma_2) (1 + x_0 \sigma_1 \sigma') (1 + x_0 \sigma_2 \sigma') (1 + h_0 \sigma')$$

Each of these partition functions can be expressed as $Z_i(\sigma) = A_i(1 + h_i\sigma)$, which gives us:

$$\begin{aligned} A_r(1 + h_r\sigma') &= \sum_{\sigma_1, \sigma_2} A_{r+1}^2(1 + h_{r+1}\sigma_1)(1 + h_{r+1}\sigma_2)(1 + x_0\sigma_1\sigma')(1 + x_0\sigma_2\sigma')(1 + h_0\sigma') \\ &= A_{r+1}^2\{(1 + 2h_{r+1}x_0h_0 + h_{r+1}^2x_0^2) + \sigma'(h_0 + 2hr + 1x_0 + h_0h_{r+1}^2x_0^2)\} \end{aligned}$$

This gives a recursion equation for the effective field at level r due to the subtrees beyond it:

$$h_r = \frac{h_0 + 2h_{r+1}x_0 + h_0h_{r+1}^2x_0^2}{1 + 2h_{r+1}x_0h_0 + h_{r+1}^2x_0^2} \quad (3.10)$$

We are interested in the effective field deep within the graph, which is independent of the level in the tree. This fixed point effective field h^* can be obtained by solving the equation:

$$x_0^2h^{*3} + (2x_0h_0 - h_0x_0^2)h^{*2} + (1 - 2x_0)h^* - h_0 = 0 \quad (3.11)$$

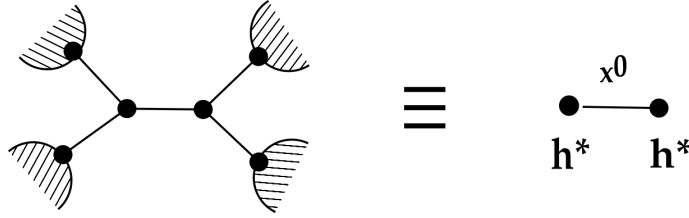


Figure 3.7: Magnetization per site in the presence of external magnetic field.

The magnetization per site can then be expressed in terms of h^* using the picture shown in Fig. 3.7 :

$$\begin{aligned} \langle \sigma_1 \rangle &= \frac{\sum_{\sigma_1, \sigma_2} \sigma_1 A^2(1 + h^*\sigma_1)(1 + h^*\sigma_2)(1 + x_0\sigma_1\sigma_2)}{\sum_{\sigma_1, \sigma_2} A^2(1 + h^*\sigma_1)(1 + h^*\sigma_2)(1 + x_0\sigma_1\sigma_2)} \\ \implies M &= \frac{h^*(1 + x_0)}{1 + h^{*2}x_0} \end{aligned} \quad (3.12)$$

The derivative of the magnetic susceptibility with respect to this effective field is

$$\frac{dM}{dh^*} = \frac{-(x_0 + 1)(x_0h^{*2} - 1)}{(x_0h^{*2} + 1)^2} \quad (3.13)$$

Since the susceptibility is the first order derivative of the magnetization with respect to the external field, we only require our equations to be first order in h_0 . We can linearize the

cubic equation 3.11 by writing $h^* = y + Bh_0$, where y is simply the value of h^* in the absence of external magnetic field h_0 . Terms involving higher orders of h_0 are ignored.

$$h_0(3Bx_0^2y^2 - 2Bx_0 + B - x_0^2y^2 + 2x_0y^2 - 1) + y(x_0^2y^2 - 2x_0 + 1) = 0$$

We then simply solve for B :

$$B = \frac{dh^*}{dh_0} = \frac{1 + x_0^2y^2 - 2x_0y^2}{3x_0^2y^2 - 2x_0 + 1} \quad (3.14)$$

We can now calculate the magnetic susceptibility:

$$\chi = \frac{1}{kT} \frac{dM}{dh_0} = \frac{1}{kT} \frac{dM}{dh^*} \frac{dh^*}{dh_0} \quad (3.15)$$

For $T \geq T_c$, we know that $y = 0$. The high temperature magnetic susceptibility χ_+ is then:

$$\chi_+ = \frac{1}{kT} \frac{1 + x_0}{(1 - 2x_0)} \quad (3.16)$$

For $T \leq T_c$, $y^2 = \frac{2x_0 - 1}{x_0^2}$ and hence the low temperature magnetic susceptibility χ_- is:

$$\chi_- = \frac{1}{kT} \frac{(1 + x_0)(1 - x_0)^3}{(2x_0 - 1)(3x_0 - 1)^2} \quad (3.17)$$

From Eq. 3.16 and Eq. 3.17, it is clear that the magnetic susceptibility diverges at the critical point $x_0 = \frac{1}{2}$.

All the expressions that we have derived here are valid on the Bethe lattice. The RLTL, as discussed earlier, locally looks like a tree upto distance $\mathcal{O}[\log S]$ from a site. In the limit that the number of sites goes to infinity, the RLTL would behave the same way as the Bethe lattice. For RLTLs with a finite number of sites, we expect to see deviations from this behaviour, which opens up the question of how measured quantities vary with the size of the lattice. Before we look at how the Ising model on the RLTL behaves and dive into the question of finite-size effects, we briefly recap the standard finite-size scaling theory.

3.1.5 Standard finite-size scaling arguments

Singularities at the critical point only occur for systems of infinite size. For systems of finite sizes, quantities near the critical point behave differently from what is expected in the thermodynamic limit. The theory of finite-size scaling, developed by Fisher and Barber [27], [28] systematically addresses how the finite size of the system modifies the behaviour of thermodynamic quantities near the critical point. A detailed historical overview of this question is given in the review article Ref. [29] by Barber. The central idea to the theory is that near the critical point, the behaviour of the system is controlled by the scaling variable ξ/L , where ξ is the correlation length. In this section, we summarize the scaling form we expect to observe for the magnetic susceptibility and the specific heat capacity. For the magnetic susceptibility, we expect to observe a scaling of the form:

$$\chi(\varepsilon, L) = \chi(\varepsilon, \infty) g(\xi/L) = \chi(\varepsilon, \infty) f(\varepsilon L^b)$$

where $\varepsilon = \frac{T-T_c}{T_c}$.

For small ε , we can write the scaling relation as:

$$\chi(\varepsilon, L) = \varepsilon^{-a} f(\varepsilon L^b) \tag{3.18}$$

In the limit that $\varepsilon \rightarrow 0$ and $L \rightarrow \infty$, we know that the magnetic susceptibility diverges. This means the function $f(\varepsilon L^b)$ tends to a finite value in this limit, implying that $\varepsilon \sim L^{-b}$. Substituting this in the scaling equation gives us:

$$\chi(\varepsilon, L) = L^{a/b} f(\varepsilon L^b) \tag{3.19}$$

The scaling function f can be found by plotting $\chi(\varepsilon, L).L^{-a/b}$ vs $\varepsilon.L^b$

In case of the Bethe lattice, the specific heat capacity does not show a divergence. We can pull out the universal finite size effects, and subtract the non-universal “analytic background”. While studying the scaling for the specific heat capacity, we work with a quantity ΔC_v which removes this analytical background and is expected to show universality:

$$\Delta C_v(L, T) = C_v(L, T) - C_v(\infty, T) \tag{3.20}$$

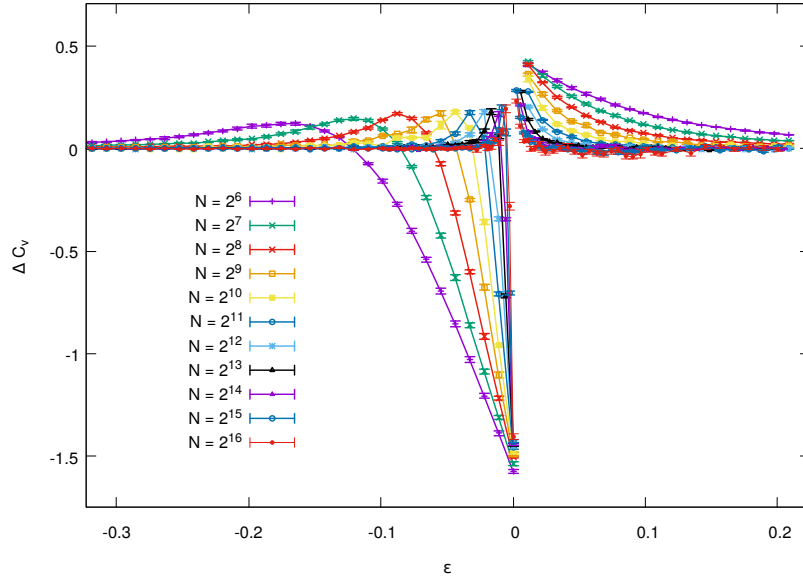


Figure 3.8: Difference between the observed and theoretical values of the specific heat per site (ΔC_v) as a function of ε for the three-coordinated RLTL with a single bilayer.

Fig. 3.8 shows a plot of ΔC_v as a function of temperature for the various lattice sizes analyzed. The arguments for the scaling of ΔC_v can be made along similar lines to the arguments made for χ . In the limit of $\varepsilon \rightarrow 0$ and $L \rightarrow \infty$, the specific heat has a discontinuity but does not diverge. This implies that $a = 0$. Hence, we expect ΔC_v to obey a scaling of the form:

$$\Delta C_v(\varepsilon, L) = \tilde{f}(\varepsilon L^b) \quad (3.21)$$

The scaling function \tilde{f} can be found by plotting ΔC_v vs $\varepsilon \cdot L^b$

3.2 Monte Carlo studies of the Ising model on the RLTL

To numerically measure the various quantities in the Ising model on RLTL, we have to obtain samples of spin configurations using Monte Carlo simulations. The most common method to do this is using the Metropolis-Hastings algorithm [14] which involves single-spin

flip dynamics. The basic idea is to start out with an arbitrary initial configuration and then at each step flip one randomly selected spin with certain probability. If flipping the spin leads to a configuration with lower energy, it is accepted with probability 1. If not, it is accepted with probability $e^{E_i - E_f/T}$, where E_i and E_f are the energies of the configuration before and after the flipping the said spin.

The single-spin flip dynamics has the issue of critical slowing down near T_c for lattices of large sizes. An algorithm that overcomes this issue is the Wolff algorithm introduced by Ulli Wolff [30]. We make use of this algorithm for our study and discuss its implementation in the next section.

3.2.1 Wolff Algorithm

The Wolff algorithm involves flipping clusters of spins and not single spins. Ref. [31] contains a good description of the working of this algorithm. We briefly discuss it here: the idea is to build a cluster from a randomly sampled spin. To start out, we pick a spin at random and add it to the cluster. In the subsequent steps, we look at sites which have links connecting to the spins at boundary of the cluster. If a site i on the boundary of the cluster is connected to a site j which is not already part of the cluster and the magnetization of these sites are the same (ie, $S_i = S_j$), site j is added to the cluster with probability $p = 1 - \exp(-2\beta J)$. Once the growth of the cluster is complete (ie, no new sites get added to the cluster), all spins in the cluster are flipped.

This algorithm is a rejection-free and is currently the fastest known method to simulate the Ising model. Note that in the limit of high temperature (in the paramagnetic phase), the Wolff algorithm effectively behaves the same way as the single-spin flip algorithm. In the low temperature region (the ordered phase), the size of the cluster is nearly the size of the lattice itself.

3.2.2 Details of implementation

This subsection summarizes the details of our implementation of the Wolff algorithm to study the Ising model on the three-coordinated RLTL. In all our implementations, we set

J and k_B to one. We say that one Monte-Carlo step is complete if there is a Wolff cluster of size 15 for $T \leq 2.0$ and size 30 for $T > 2.0$. In general, we use a grid size of 0.02 for the temperature. For lattices of larger size, we use a finer temperature spacing (0.01 or 0.005 as appropriate) around the critical temperature. Interestingly, in our studies, we find that the behaviour of the Ising model was dependent only on the total number of sites in the lattice and **not sensitive to the aspect ratio**. Hence, for simplicity, we take RLTL lattices with a single bilayer ($m = 2$) and number of sites in each layer of the form $N = 2^n$, where $n = 6, 7, \dots, 16$. The total number of sites in the lattice is then $2 \cdot 2^n$. Thus, the largest lattice size we have used for our simulation is of order 10^6 sites. For each lattice size, we take 20 independent realizations of the RLTL and run the Wolff algorithm. At each temperature, we first equilibrate the system for 500 Monte-Carlo steps and then collect data for 5×10^4 Monte-Carlo steps. For larger sizes ($S \geq 2^{15}$), there is a self-averaging of the different quantities and we can thus reduce the required number of Monte-Carlo samples to 2.5×10^4 . We report our results after averaging over these 20 independent RLTL realizations (which corresponds to at least 5×10^5 Monte-Carlo samples in total) with error bars equal to the standard error.

3.2.3 Numerically calculating the magnetic susceptibility for finite systems

If we plot the probability distribution of the magnetization for *finite* systems at $T > T_c$, we see that this distribution has a single peak around $m = 0$. For $T < T_c$, this distribution is peaked at two values of m — one positive and one negative. In fact, as we increase the system size, these distributions become more sharply peaked (see Fig. 3.9). As a result of this double peak at $T < T_c$, the average value of the magnetization per site averaged over a large number of samples ends up being zero even in the ordered phase.

In the thermodynamic limit however, the magnetization of the system stays in one peak even for $T < T_c$. A detailed description of this symmetry-breaking of m in the thermodynamic limit is given in Ref. [32]. To understand why this happens, we have to look at the time series for the magnetization generated by the Monte-Carlo simulations of the Ising model. As the size of the system increases, the time taken for the magnetization of the system to flip signs (ie, move from one peak to the other) increases. Hence, in the thermodynamic limit, the system essentially stays peaked around a single value of m . Recall that

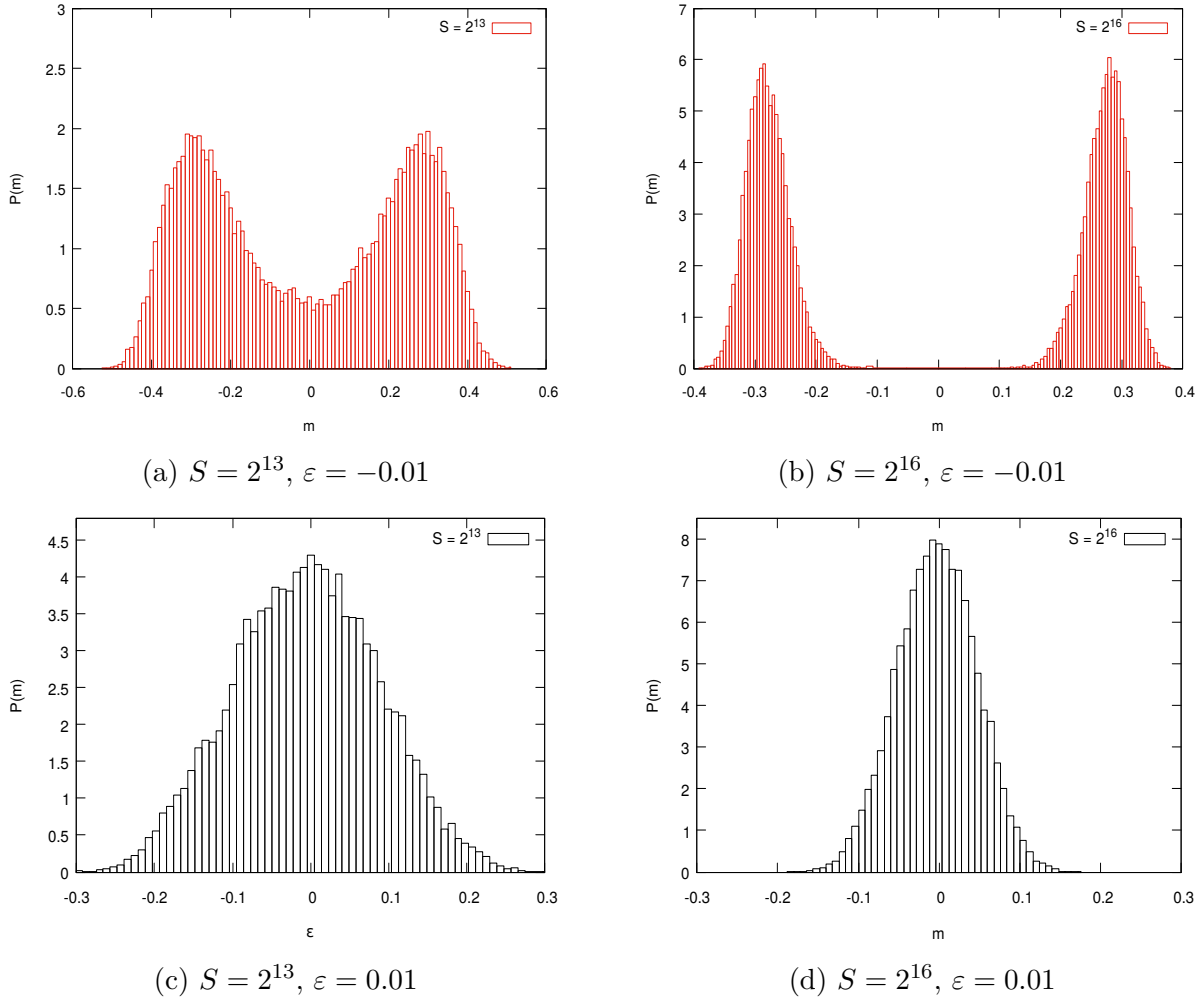


Figure 3.9: Probability density distribution of the magnetization per site for RLTLs of size $S = 2^{13}$ and 2^{16} respectively. For $T \leq T_c$, the distribution of the magnetization has two peaks. For $T > T_c$, the distribution of the magnetization is a single peak centred around $m = 0$. As the size of the system increases, the peaks get sharper.

all our theoretical expressions are only valid in this thermodynamic limit.

To avoid the issue of the magnetization having a double-peak in finite systems, we work with the *absolute* value of the magnetization instead. This corresponds to “folding” the distributions of the magnetization along the $y = 0$ axis. For $T < T_c$, we then end up with a single-peaked distribution. Note that in the region above T_c , the distribution of $\langle |m| \rangle$ ends up being a half normal which is not symmetric around $m = 0$. To relate the variance of $\langle |m| \rangle$ for lattices of smaller sizes at $T > T_c$ to the theoretical expressions (the thermodynamic limit), we have to introduce a multiplicative factor of ≈ 0.36 . This factor becomes insignificant for

lattices of larger size where the distribution of m is very sharply peaked and $\langle |m| \rangle$ tends to zero.

3.2.4 Results of Monte Carlo studies on the RLTL

Energy per site

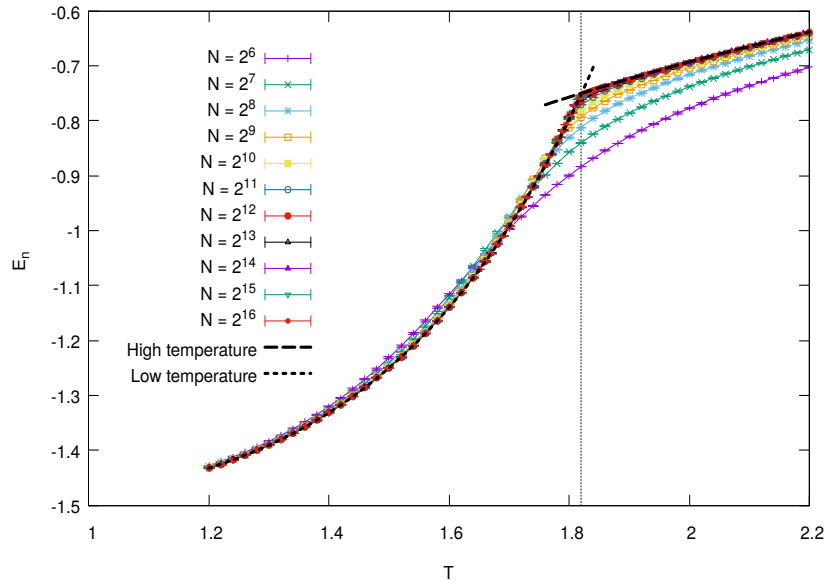


Figure 3.10: Energy per site as a function of temperature for the three-coordinated RLTL with a single bilayer for different values of N . The dashed line is the theoretically expected curve (given by Eq. 3.8). The vertical line denotes the critical temperature T_c . The maximum error bar is of order 10^{-4} for $N \geq 8$ and order 10^{-3} for $N < 8$.

Fig. 3.10 shows a plot of the average energy per site as a function of temperature for lattices of different sizes for an RLTL with a single bilayer. The theoretically expected function (given by Eq. 3.8) is shown using a dashed curve. As seen, for larger lattice sites, the Monte-Carlo simulations are in good agreement with the theory. For the lattices of smaller size ($N \leq 2^{11}$), we observe significant deviations above the critical temperature. However, for temperatures far away from the critical temperature ($T \geq 2.5$), the data agrees well with the theory even for the smaller sizes (not shown in the figure). For lattices of sizes $S = 2^8, 2^9$ the maximum error bar is of order 10^{-3} . For larger sizes, the maximum error bars are of order 10^{-4} — primarily in the high temperature region where the size of the Wolff

clusters are small. Around the critical point, the errors are of order 10^{-5} for these lattices.

Absolute magnetization per site

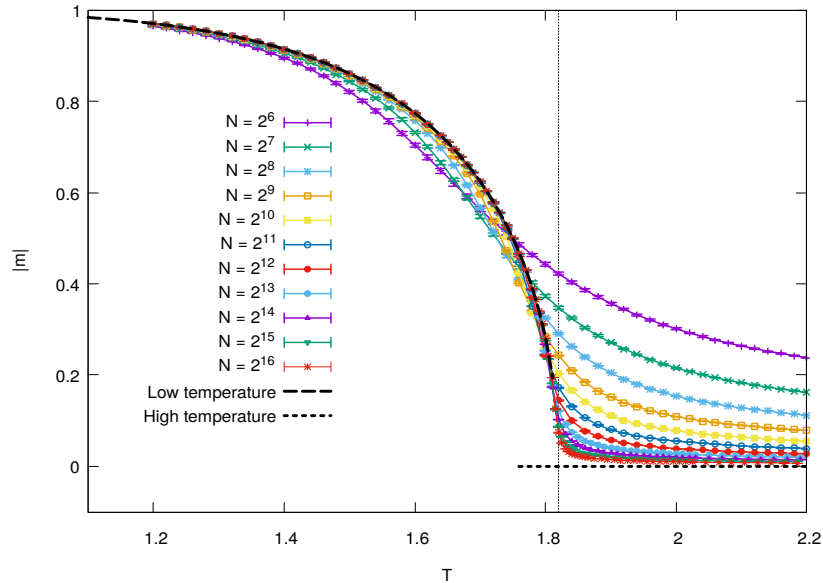


Figure 3.11: Absolute magnetization per site as a function of temperature for the three-coordinated RLTL with a single bilayer for different values of N . The dashed line is the theoretically expected curve for the Bethe lattice (given by Eq. 3.7). The vertical line is at the critical temperature T_c .

As discussed previously in subsection 3.2.3, it is best to work with the absolute value of magnetization. Fig. 3.11 shows a plot of the absolute value of the magnetization per site as a function of temperature. The dashed line corresponds to the absolute value of Eq. 3.7, which is what we expect from theory. For lattices with $S \leq 2^{10}$, the maximum error in $|m|$ occurs around critical point and is of order 10^{-3} . Lattices with $S > 2^{10}$ had a maximum error of order 10^{-4} around the critical point.

Specific heat capacity

The specific heat capacity can be calculated from the Monte-Carlo data using the following relation:

$$C_v = N \frac{\langle e^2 \rangle - \langle e \rangle^2}{T^2} \quad (3.22)$$

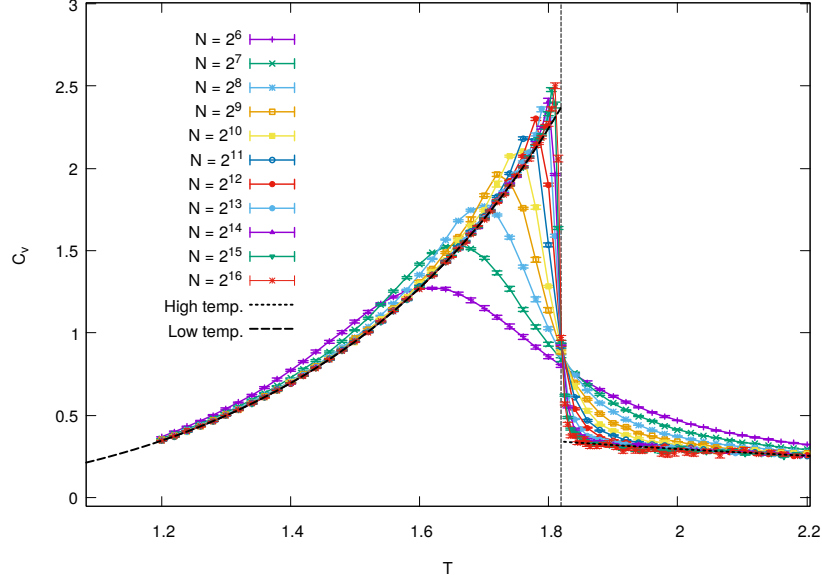


Figure 3.12: Specific heat capacity per site as a function of temperature for the three-coordinated RLTL with a single bilayer for different values of N . The dashed line is the theoretically expected curve (given by Eq. 3.9). The vertical line is at the critical temperature T_c .

Fig. 3.12 shows the results from our simulations. For lattices of finite size, we do not observe a discontinuity in C_v . As we increase the size of the lattice, the plot of C_v tends towards the theoretically expected curve and the jump becomes apparent. For lattices of size $S < 2^{12}$, the error bars are of order 10^{-3} . For lattices of size $S \geq 2^{12}$, the error at the peak value of C_v is ~ 0.01 and of order 10^{-3} everywhere else.

Magnetic Susceptibility

To measure the magnetic susceptibility from our data, we find convenient to work with a quantity that depends on the variance of $|M|$ and not variance of M . This is not same as the magnetic susceptibility. In the thermodynamic limit however, in the low temperature ordered phase this quantity agrees with the magnetic susceptibility. In the high temperature phase, it differs by a multiplicative constant (discussed previously in Sec. 3.2.3). For finite N , there is a smearing near T_c , and the finite size effect is **not** same as the usual susceptibility, but qualitatively similar. The “absolute” magnetic susceptibility is define as:

$$\chi_{abs} = N \frac{\langle m^2 \rangle - \langle |m| \rangle^2}{T} \quad (3.23)$$

The plot of this measured magnetic susceptibility is shown in Fig. 3.13. Since we are working with lattices of finite size, χ_{abs} does not diverge at T_c . The value of the peak however, increases sharply as the lattice size increases. Across all lattice sizes, the maximum error in χ_{abs} occurs at the peak and the percentage error at this data point is of order 0.1%.

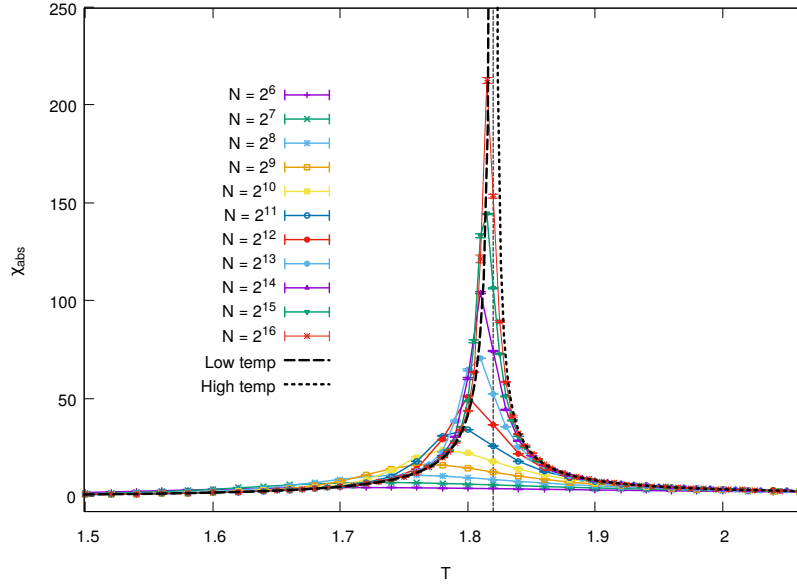


Figure 3.13: Magnetic susceptibility per site as a function of temperature for the three-coordinated RLTL with a single bilayer for different values of N . The dashed line is the theoretically expected curve (given by Eq. 3.16 and 3.17). The vertical line denotes the critical temperature T_c .

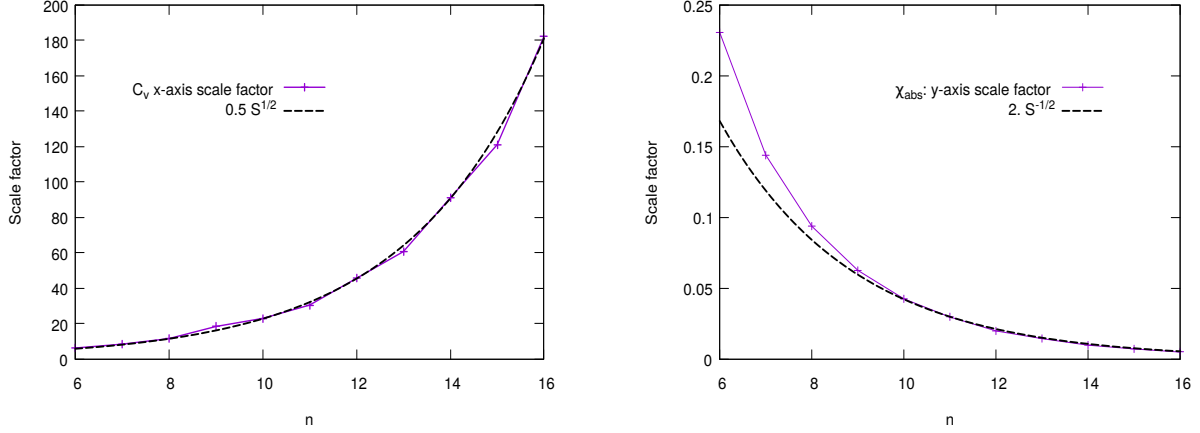
3.3 Finite-size scaling on the RLTL

In the limit of the number of sites going to infinity, we expect the Ising model on the RLTL to be exactly what is expected on the Bethe lattice. However, as we have seen, for finite sizes, there is a deviation from the behaviour expected in this limit. Do these deviations scale systematically with the size of the lattice as predicted by the standard finite-size scaling hypothesis? In other words, the problem now is to see if we can find an appropriate ‘L’ that appears in the scaling variable in Eqs. 3.19 and 3.21 for the RLTL. In general, a finite system of volume V in d dimensions can be characterized by a length scale $L \propto V^{1/d}$. For a lattice with total number of sites S , we can consider the volume to be proportional to S . Within the locally tree-like approximation, we note that the RLTL is “infinite” dimensional and when d becomes large, $S^{1/d}$ is $\sim \log(S)$. We also saw that different measures of the size of the graph — such as the average diameter and the radius of gyration — were linear in $\log(S)$. So our initial naive guess is that ‘L’ is $\log(S)$. However, on trying to use this in the scaling variable for our Monte-Carlo data, we were unable to obtain a satisfactory collapse.

To study this more systematically, we manually scale the axes in the plots of ΔC_v and χ so that the positions and heights of the peak match for all lattice sizes. We can then study how this scale factor depends on S to understand what scaling variable to use. Consider the plot of ΔC_v given in Fig. 3.8: we observe that for lattices of size $N \geq 2^{11}$, the heights of the peak are the same. This is consistent with Eq. 3.21 which suggests that the y-axis does not require scaling. We then simply scale the x-axis so that the position of this peak is the same for all sizes and plot the scale factor as a function of n (recall that the total number of sites in the lattice is of the form 2.2^n). Fig. 3.14a shows the x-axis scale factors for ΔC_v . Similarly, we obtain the scale factors for the x and y axes of the magnetic susceptibility. Fig. 3.14b shows the scale factors used for the y-axis of the susceptibility plots as a function of n . We observe that the scale factors are proportional to $S^{1/2}$.

If we plot ΔC_v as a function of the reduced temperature ε and scale the x-axis by $S^{1/2}$, (ie, using $L = S$ and $b = 0.5$ in Eq. 3.21), we find that we are able to obtain a good collapse for different lattice sizes as shown in Fig. 3.15.

On plotting the magnetic susceptibility χ as a function of ε and scaling the x-axis by $S^{1/2}$, we find that the positions of all the peaks coincide. On scaling the y-axis by a factor



(a) Scale factor used for the x-axis for C_v . (b) Scale factor for the y-axis peaks of χ_{abs} .

Figure 3.14: Scale factors used to collapse the peaks in the C_v and χ plots to the same point.

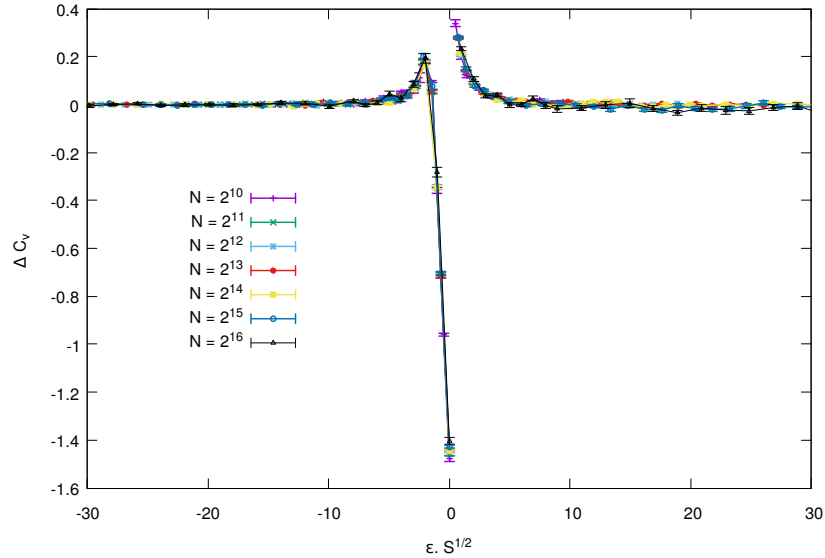


Figure 3.15: Scaling collapse for ΔC_v vs ϵ .

$S^{-1/2}$, we were able to obtain a collapse for the heights of the peak as well, as shown in Fig. 3.16. This scaling corresponds to using $L = S, b = 0.5$ and $a = -1$ in Eq. 3.19. However, we note that the region below $\epsilon \cdot S^{1/2} = -5$ appears to have significant corrections to scaling. We will study this in more detail subsequently.

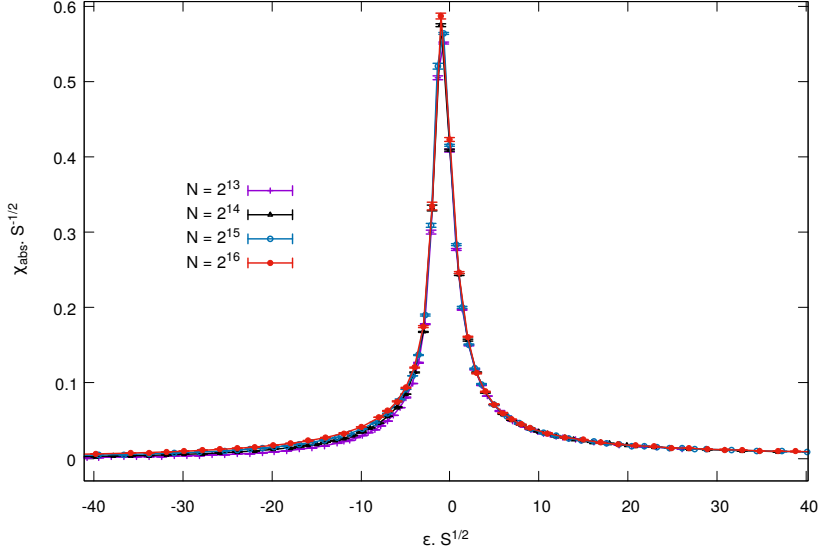


Figure 3.16: Scaling collapse for χ vs ε .

3.4 Theory for finite-size scaling of the Ising model on the RLTL

We verified that the same scaling variables work for RLTLs of coordination number four as well by performing Monte-Carlo studies of the Ising model on the four-coordinated lattice defined in Chapter 1 (a representative plot shown for χ_{abs} in Fig. 3.17). To explain the observed scaling behaviour, we postulate that near the critical point, the probability distribution of the magnetization follows the form predicted by Landau Theory [33], [34].

Let $M = \sum_i \sigma_i$ be the total magnetization of the system. As per Landau theory, the probability distribution of M in the region near T_c is given by:

$$P(M) = \mathcal{N} \exp\left(-\frac{a\varepsilon M^2}{S} - \frac{bM^4}{S^3}\right) \quad (3.24)$$

where a and b are constants that are independent of the number of sites and the temperature. They would however, depend on the details of the lattice (in our case, the coordination number). \mathcal{N} is the normalization constant.

As a consistency check, we fit the probability distribution of the magnetization per site

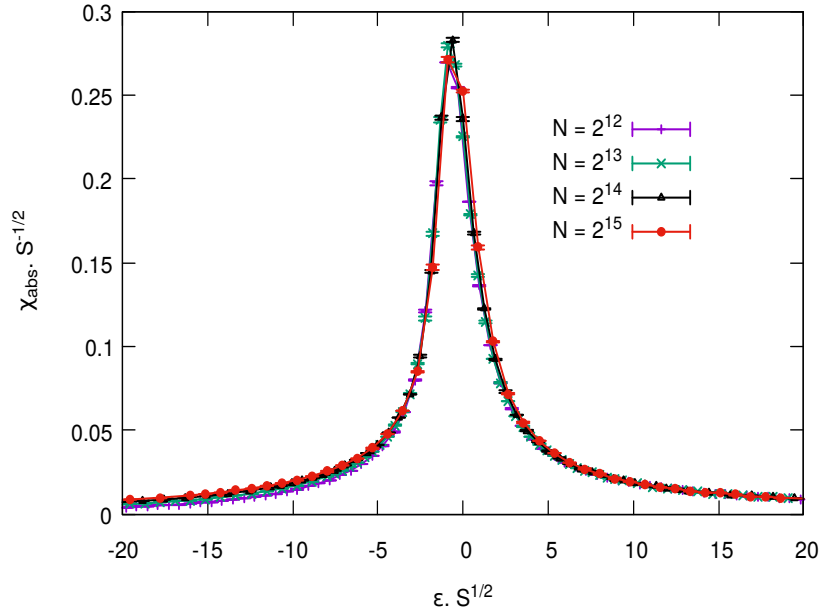


Figure 3.17: Scaling collapse for the magnetic susceptibility for the **four-coordinated** RLTL with a single layer.

near the critical point from our Monte-Carlo data of the Ising model on the RLTL to the form in Eq. 3.24 to ensure that we do indeed obtain a value of a and b that is independent of T and S . Representative plots are shown in Fig. 3.18.

Why do we expect this form to be valid on the RLTL?

Why would the Landau form of the probability distribution of the magnetization give us the expected scaling behaviour for the Ising model on the RLTL? We suggest that under renormalization, the Hamiltonian of the nearest neighbour Ising model on the RLTL flows to the Hamiltonian of the mean-field Ising model.

Consider the three-coordinated RLTL. Since the lattice is locally tree-like, we can define a block of spins of size four as shown by the labelled sites in the left picture in Fig. 3.19. Consider a maximal cover of such blocks on the RLTL. We then renormalize these block by assigning a spin variable to each block. Fig. 3.19 shows the first step of this renormalization, the result being a coupling between blocks and an effective increase in the coordination num-

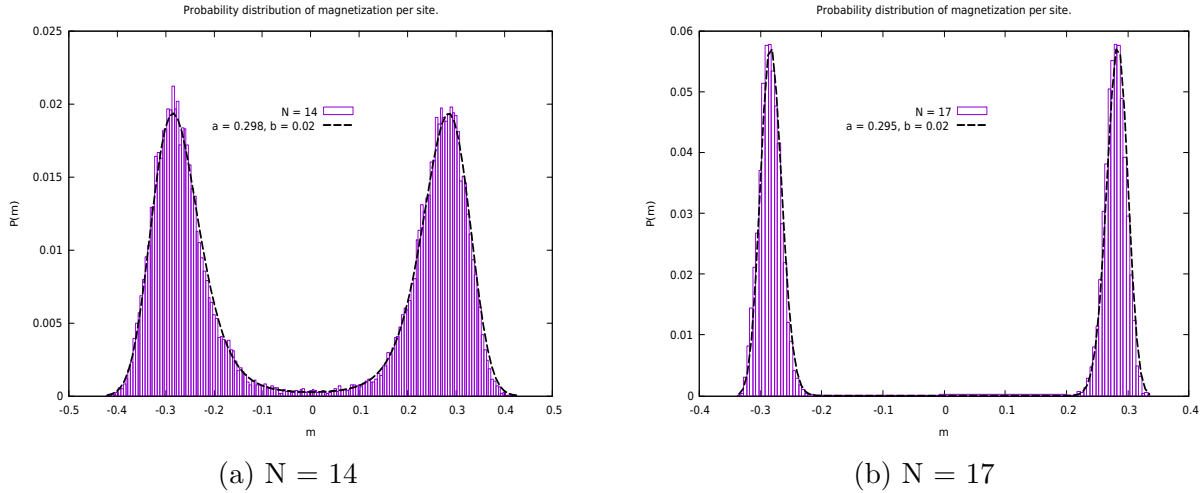


Figure 3.18: Fitting the probability distribution of m to the Landau form in Eq. 3.24 for the three-coordinated RLTL. We obtain a value of $a = 0.29$ and $b = 0.02$.

ber. So under a single step of renormalization, the original short-ranged (nearest-neighbour) Ising model Hamiltonian renormalizes to a Hamiltonian with a higher coordination number.

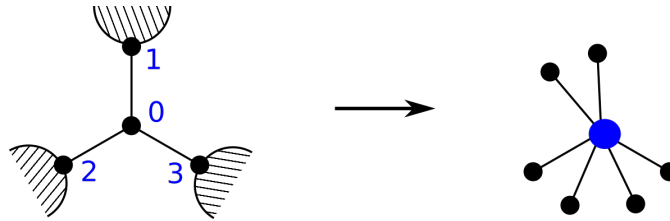


Figure 3.19: First step of renormalization of a block of spins of size four on the three-coordinated RLTL.

After each step of renormalization, the coordination number becomes much higher (in the case of the three-coordinated RLTL, the coordination number increases by a factor of two after every step). Eventually, we expect to reach a fixed point Hamiltonian (\mathcal{H}^*) in which all the spins are coupled to each other given by Eq. 3.25. So, we expect this fixed point (mean-field) Hamiltonian to govern the behaviour of our system.

The Hamiltonian for the long-ranged mean-field Ising model is:

$$\mathcal{H}^* = -\frac{J}{S} \left(\sum_i \sigma_i \right)^2 \quad (3.25)$$

In this case, each spin couples with all other spins in the graph with equal strength.

If M is the total magnetization of the system, the partition function of this system can be written in terms of M as:

$$Z_S(\beta) = \sum_M \left(\frac{S}{\frac{S+M}{2}} \right) e^{\beta JM^2/S} \quad (3.26)$$

Around T_c , the expected value of M is very small and so Eq. 3.26 can be approximated to be of the following form, which is the same as that predicted by Landau theory:

$$Z_S(\beta) = \int_{-\infty}^{\infty} \exp \left(-\frac{a\varepsilon M^2}{S} - \frac{bM^4}{S^3} \right) dM \quad (3.27)$$

In summary, we expect the Ising model on the RLTL to follow the behaviour predicted by Landau theory near the critical point. The suggested justification for why this is true is that the Ising model on the RLTL under renormalization “flows” to the mean-field Ising model.

We can now use this form of the probability distribution of M to derive the *exact* expression for the scaling functions near T_c . Let us absorb all the constants and define new re-scaled variables \tilde{M} and $\tilde{\varepsilon}$. Once we obtain the scaling function in terms of these re-scaled variables, we can scale the x and y axes appropriately to recover the constants a and b .

$$\frac{bM^4}{S^3} = \frac{\tilde{M}^4}{4} \quad \text{and} \quad \frac{a\varepsilon M^2}{S} = \frac{\tilde{M}^2 \tilde{\varepsilon}}{2}$$

The probability distribution can be written in terms of these new variables as:

$$P(\tilde{M}) \propto \exp \left(-\frac{\tilde{\varepsilon} \tilde{M}^2}{2} - \frac{\tilde{M}^4}{4} \right) \quad (3.28)$$

We define the re-scaled partition function $Z(\tilde{\varepsilon})$:

$$Z(\tilde{\varepsilon}) = \int_{-\infty}^{\infty} \exp \left(-\frac{\tilde{\varepsilon} \tilde{M}^2}{2} - \frac{\tilde{M}^4}{4} \right) dM \quad (3.29)$$

From this, it is straightforward to obtain the form of the scaling function **near** T_c for χ and ΔC_v .

Calculating the theoretical scaling functions

Near T_c , the magnetic susceptibility can be approximated to be

$$\chi \approx \frac{\langle M^2 \rangle - \langle |M| \rangle^2}{ST_c}$$

First, we show that the probability distribution for the magnetization given by Eq. 3.24 gives us the correct scaling form that we expect for the susceptibility. Each of the expectation values appearing in the equation for the susceptibility can be explicitly calculated using this probability distribution:

$$\begin{aligned} \langle M^2 \rangle &= \frac{\int_{-\infty}^{\infty} M^2 \exp\left(-\frac{a\varepsilon M^2}{S} - \frac{bM^4}{S^3}\right) dM}{\int_{-\infty}^{\infty} \exp\left(-\frac{a\varepsilon M^2}{S} - \frac{bM^4}{S^3}\right) dM} = \frac{S^{3/2}}{2b^{1/2}} \frac{\int_{-\infty}^{\infty} \tilde{M}^2 \exp\left(-\frac{\tilde{\varepsilon}\tilde{M}^2}{2} - \frac{\tilde{M}^4}{4}\right) d\tilde{M}}{\int_{-\infty}^{\infty} \exp\left(-\frac{\tilde{\varepsilon}\tilde{M}^2}{2} - \frac{\tilde{M}^4}{4}\right) d\tilde{M}} \\ \langle |M| \rangle^2 &= \left[\frac{\int_{-\infty}^{\infty} 2M \exp\left(-\frac{a\varepsilon M^2}{S} - \frac{bM^4}{S^3}\right) dM}{\int_{-\infty}^{\infty} \exp\left(-\frac{a\varepsilon M^2}{S} - \frac{bM^4}{S^3}\right) dM} \right]^2 = \frac{S^{3/2}}{2b^{1/2}} \left[\frac{\int_{-\infty}^{\infty} 2\tilde{M} \exp\left(-\frac{\tilde{\varepsilon}\tilde{M}^2}{2} - \frac{\tilde{M}^4}{4}\right) d\tilde{M}}{\int_{-\infty}^{\infty} \exp\left(-\frac{\tilde{\varepsilon}\tilde{M}^2}{2} - \frac{\tilde{M}^4}{4}\right) d\tilde{M}} \right]^2 \end{aligned}$$

And so using these expressions, the susceptibility can be written in the form

$$\chi = \frac{\langle M^2 \rangle - \langle |M| \rangle^2}{ST_c} = S^{1/2} h(\tilde{\varepsilon})$$

Recalling that $\tilde{\varepsilon} = \frac{a}{b^{1/2}} \varepsilon S^{1/2}$, we obtain the expected scaling form:

$$\chi S^{-1/2} = f(\varepsilon S^{1/2})$$

It turns out that for $\tilde{\varepsilon} > 0$ we can write down an actual functional form for the scaling function. In this region, the re-scaled partition function given in Eq. 3.29 can be expressed

in terms of the Bessel function of fractional order [35]:

$$Z(\tilde{\varepsilon}) = \frac{\sqrt{\tilde{\varepsilon}} \exp\left(\frac{\tilde{\varepsilon}^2}{8}\right) K_{\frac{1}{4}}\left(\frac{\tilde{\varepsilon}^2}{8}\right)}{\sqrt{2}}, \quad \tilde{\varepsilon} > 0 \quad (3.30)$$

In fact, for $\tilde{\varepsilon} > 0$, the entire scaling function near T_c can be expressed in terms of the Bessel function of fractional order and the error function [35]. Calculating the expectation values of \tilde{M}^2 and $|\tilde{M}|$ using the partition function, we get:

$$\langle \tilde{M}^2 \rangle = 2 \frac{d \ln Z(\tilde{\varepsilon})}{d \tilde{\varepsilon}} = \frac{1}{2} \tilde{\varepsilon} \left(\frac{K_{\frac{3}{4}}\left(\frac{\tilde{\varepsilon}^2}{8}\right)}{K_{\frac{1}{4}}\left(\frac{\tilde{\varepsilon}^2}{8}\right)} - 1 \right) \quad ; \quad |\langle \tilde{M} \rangle| = \frac{\sqrt{2\pi} \exp\left(\frac{\tilde{\varepsilon}^2}{8}\right) \operatorname{erfc}\left(\frac{\tilde{\varepsilon}}{2}\right)}{\sqrt{\tilde{\varepsilon}} K_{\frac{1}{4}}\left(\frac{\tilde{\varepsilon}^2}{8}\right)}$$

We define a universal quantity $\tilde{\chi}$ as:

$$\tilde{\chi} = \langle \tilde{M}^2 \rangle - \langle |\tilde{M}| \rangle^2 \quad (3.31)$$

$$\Rightarrow \tilde{\chi} = \frac{1}{2} \tilde{\varepsilon} \left(\frac{K_{\frac{3}{4}}\left(\frac{\tilde{\varepsilon}^2}{8}\right)}{K_{\frac{1}{4}}\left(\frac{\tilde{\varepsilon}^2}{8}\right)} - 1 \right) - \frac{2\pi e^{\frac{\tilde{\varepsilon}^2}{4}} \left(\operatorname{erfc}\left(\frac{\tilde{\varepsilon}}{2}\right) \right)^2}{\tilde{\varepsilon} \left(K_{\frac{1}{4}}\left(\frac{\tilde{\varepsilon}^2}{8}\right) \right)^2} \quad (3.32)$$

For $\tilde{\varepsilon} < 0$ we were unable to find a functional form for the partition function and $\tilde{\chi}$, and hence resort to calculating the functions numerically. Note that the universal scaling function $\tilde{\chi}$ defined above does not depend on the coordination number of the lattice — ie, it is independent of a and b . The *actual* scaling function for the magnetic susceptibility $f(\varepsilon S^{1/2})$ is related to $\tilde{\chi}$ by re-scaling the axes in the plot of $\tilde{\chi}$ as a function of $\tilde{\varepsilon}$. The x-axis should be re-scaled by a factor $\frac{b^{1/2}}{a}$ and the y-axis by a factor $\frac{1}{2T_c b^{1/2}}$.

We now check whether this theoretical scaling function agrees with our Monte-Carlo data. Fig. 3.20 shows the plot of the theoretical scaling function after rescaling the axes to obtain the best possible match to the data. This re-scaling was done separately for $\varepsilon > 0$ and $\varepsilon < 0$. Relating the scale factors of the axes to a and b , we find that: for $\varepsilon < 0$, the values of a and b are (0.289, 0.019) while for $\varepsilon > 0$, the values are (0.275, 0.018).

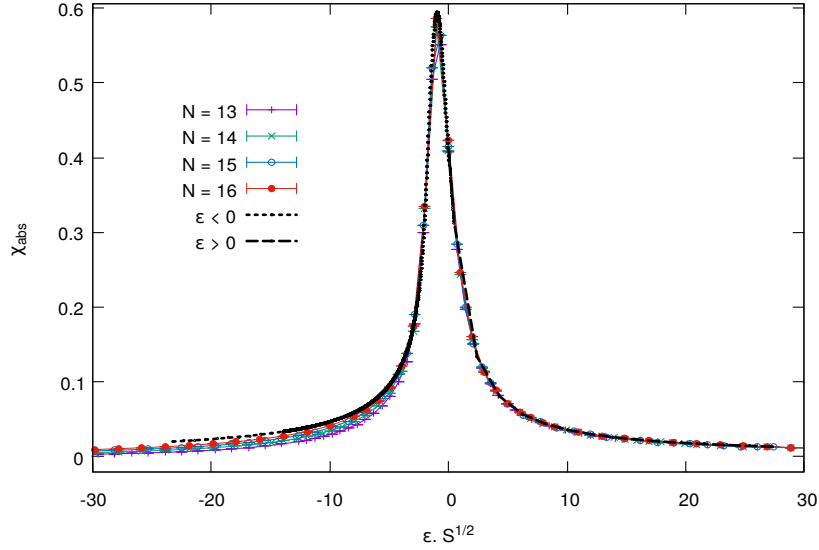


Figure 3.20: Theoretical scaling function for the magnetic susceptibility.

3.5 Corrections to scaling

While this theory seems to give us the asymptotic scaling function, there are significant corrections to this theoretical scaling form for $\varepsilon S^{1/2} < -5$ (this corresponds to $\varepsilon \sim -0.02$). We claim that these corrections can be explained by introducing a first order temperature dependence in the coefficient of M^4 in the free energy.

$$F(M) = \frac{a\varepsilon M^2}{S} + (b + d\varepsilon) \frac{M^4}{S^3}$$

where d is another constant.

In terms of the re-scaled variables $\tilde{M} = M/S^{3/4}$ and $\tilde{\varepsilon} = \varepsilon/S^{1/2}$, this is:

$$F(\tilde{M}) = a\tilde{\varepsilon}\tilde{M}^2 + \left(b + \frac{d\tilde{\varepsilon}}{S^{1/2}}\right)\tilde{M}^4$$

From this, we expect the deviations from the asymptotic scaling function to be of the form $S^{-1/2}$. This can be tested using our data. We plot the difference between value of the observed scaling function and the theoretically expected scaling function at $\varepsilon S^{1/2} = -10$ as a function of lattice size to check whether the corrections scale as $S^{-1/2}$. From Fig. 3.21 we see that this correction term agrees with the observed deviations.

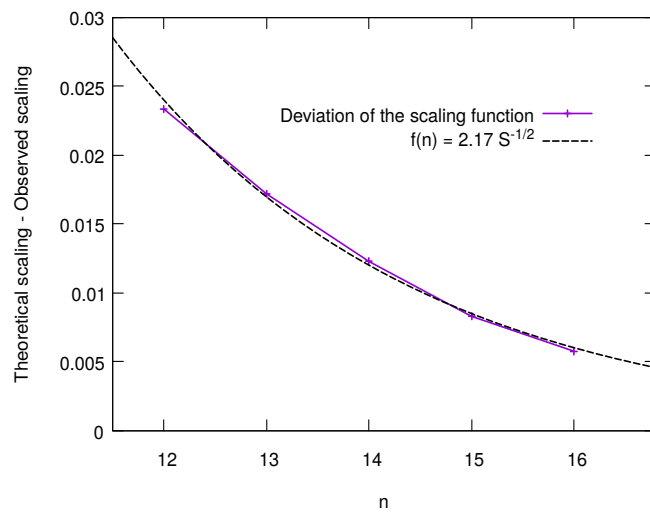


Figure 3.21: Difference between the observed scaling function and the theoretical (asymptotic) scaling function at $\varepsilon S^{1/2} = -10$ as a function of N (recall that the number of sites per layer is 2^N). The dashed line is the function $S^{-1/2}$.

Chapter 4

Summary

We have defined a variation of a random regular graph called the Random Locally Tree-Like Layered Lattice (RLTL). For large number of sites S , we argued that the shortest loop passing through a random site on this graph is of order $\mathcal{O}[\log_{r-1} S]$, where r is the coordination number of the graph. This implies that upto $\mathcal{O}[\log_{r-1} S]$, the lattice locally looks like a branching tree. The Bethe approximation thus becomes exact on this lattice when the total number of sites goes to infinity. Since this lattice is regular, it avoids the issue of subtracting any surface corrections. Numerical studies are also feasible on this graph since it is finite and does not need these corrections. Thus, some models in statistical physics become more tractable to study on the RLTL. In particular, while the finite-size corrections to the Ising model on random graphs in thermodynamic limit has not been well-studied in previous literature, we are able to explicitly calculate the finite-size scaling functions for this model on the RLTL.

In Chapter 2, we probed the geometrical structure of the RLTL. We found that the sample-averaged diameter of the RLTL is linear in the logarithm of the total number of sites S to leading order in S . The plot of the sample-averaged diameter as a function of $\log(S)$ showed a distinct staircase-like structure. We explained this structure by studying the sample-to-sample variation in the diameter. It was found that the distribution of the diameters across samples for RLTLs of the same size was sharply peaked and took at most three distinct values. The standard error in the diameter fluctuates between 0 and 0.5, and

the flat regions in the plot of the diameter vs $\log(S)$ corresponds to lattice sizes for which all realizations of the RLTL have the same diameter. We then defined a more smoothly behaved quantity called the radius of gyration. We found that this quantity was also linear in $\log(S)$. Using the property that the sites in a shell constructed around any site in the lattice are approximately randomly distributed, we showed that the probability distribution of the distances between sites on the lattice follows the relation:

$$P(d(u, v) \geq R) = \exp \left[-\frac{2R}{aS} \right]$$

where a is a constant of $\mathcal{O}(1)$.

In Chapter 3, we looked at the behaviour of the Ising model on the RLTL. We studied finite-size corrections of the magnetic susceptibility per site (χ) and the deviation of the specific heat capacity from the thermodynamic value ($\Delta C_v = C_v(L, T) - C_v(\infty, T)$). We obtained a scaling collapse for both these quantities with a scaling of the form:

$$\begin{aligned} \chi S^{-1/2} &= f(\varepsilon S^{1/2}) \\ \Delta C_v &= g(\varepsilon S^{1/2}) \end{aligned} \tag{4.1}$$

where $\varepsilon = \frac{T-T_c}{T_c}$.

Obtaining this scaling is particularly interesting because the specific heat capacity per site in the thermodynamic limit does not diverge at the critical point. The appearance of $S^{1/2}$ in the scaling variable is also contrary to our original naive expectation of $\log(S)$.

We have proposed a theory to explain the observed finite-size scaling behaviour. We claim that near the critical point, the probability distribution of the magnetization is of the form:

$$P(M) \propto \exp \left(-\frac{a\varepsilon M^2}{S} - \frac{bM^4}{S^3} \right)$$

where a and b are constants independent of the temperature and number of sites. Using this, we were able to explicitly obtain the form of the scaling functions that appear in Eq. 4.1 above. This theoretical form is consistent with the scaling collapse observed in our Monte-Carlo data. The corrections to this asymptotic finite-size scaling function are however noticeable for $\varepsilon < 0$. We have explained these corrections to scaling and shown that the deviations from the asymptotic scaling function are of the form $S^{-1/2}$.

Bibliography

- [1] H. A. Bethe, “Statistical theory of super lattices,” *Proc. Roy. Soc. London A*, vol. **166**, 1935.
- [2] K. R. Kurata M. and W. R., “A theory of cooperative phenomena. iii. detailed discussions of the cluster variation method,” *J. Chem. Phys.*, vol. **21**, 1953.
- [3] E. Müller-Hartmann and J. Zittartz, “New type of phase transition,” *Phys. Rev. Lett.*, vol. **33**, 1974.
- [4] T. P. Eggarter, “Cayley trees, the ising problem, and the thermodynamic limit,” *Phys. Rev. B*, vol. **9**, 1974.
- [5] H. Matsuda, “Infinite susceptibility without spontaneous magnetization: Exact properties of the ising model on the cayley tree,” *Progress of Theoretical Physics*, vol. **51**, 1974.
- [6] R. Baxter, *Exactly Solved Models in Statistical Mechanics*. Dover Publications, 1982.
- [7] D. Dhar, P. Shukla, and J. P. Sethna, “Zero-temperature hysteresis in the random-field ising model on a bethe lattice,” *Journal of Physics A: Mathematical and General*, vol. **30**, Aug. 1997.
- [8] A. Dembo and A. Montanari, “Ising models on locally tree-like graphs,” *The Annals of Applied Probability*, vol. **20**, 2010.
- [9] C. Baillie, D. Johnston, and J. Kownacki, “Ising spins on thin graphs,” *Nuclear Physics B*, vol. **432**, 1994.
- [10] D. A. Johnston and P. Plechác, “Potts models on feynman diagrams,” *Journal of Physics A: Mathematical and General*, vol. **30**, 1997.
- [11] P. Erdős and A. Rényi, “On random graphs,” *Publ. Math. Debrecen*, vol. **6**, 1959.

- [12] P. Erdős and A. Rényi, “On the strength of connectedness of a random graphs,” *Acta Math. Acad. Sci. Hungar.*, vol. **12**, 1961.
- [13] P. Erdős and A. Rényi, “On the evolution of random graphs,” *Publ. Math. Inst. Hung. Acad. Sci.*, vol. **5**, 1960.
- [14] I. Tishby, O. Biham, and E. Katzav, “The distribution of first hitting times of random walks on directed erdős–rényi networks,” *Journal of Statistical Mechanics: Theory and Experiment*, 2017.
- [15] B. Bollobás, *Random Graphs*. Cambridge University Press, 2001.
- [16] S. Janson, T. Luczak, and A. Ruciński, *Random Graphs*. John Wiley New York, 2000.
- [17] D. Dhar, R. Rajesh, and J. F. Stilck, “Hard rigid rods on a bethe-like lattice,” *Phys. Rev. E*, vol. **84**, 2011.
- [18] S. N. Dorogovtsev, A. V. Goltsev, and J. F. F. Mendes, “Critical phenomena in complex networks,” *Rev. Mod. Phys.*, vol. **80**, 2008.
- [19] S. Dommers, C. Giardinà, and R. V. D. Hofstad, “Ising critical exponents on random trees and graphs,” *Communications in Mathematical Physics*, vol. **28**, 2014.
- [20] S. N. Dorogovtsev, A. V. Goltsev, and J. F. F. Mendes, “Ising model on networks with an arbitrary distribution of connections,” *Phys. Rev. E*, vol. **66**, 2002.
- [21] A. D. Korshunov, “On the diameter of random graphs,” *Soviet Math. Dokl.*, vol. **12**, 1971.
- [22] V. Klee and D. Larman, “Diameters of random graphs,” *Canadian Journal of Mathematics*, vol. **33**, 1981.
- [23] F. Chung and L. Lu, “The diameter of sparse random graphs,” *Advances in Applied Mathematics*, vol. **26**, 2001.
- [24] J.-C. Bermond and B. Bela, “The diameter of graphs: A survey,” *Congressus Numerantium*, vol. **32**, 1981.
- [25] F. Chung, “Diameter of graphs: Old problems and new results,” *Congressus Numerantium*, vol. **60**, pp. 295–317, 1987.
- [26] B. Bollobas and W. Fernandez de la Vega, “The diameter of random regular graphs,” *Combinatorica*, vol. **2**, 1982.
- [27] M. E. Fisher, “Critical phenomena,” *Proceedings of the Enrico Fermi International School of Physics*, vol. **51**, 1971.

- [28] M. E. Fisher and M. N. Barber, “Scaling theory for finite-size effects in the critical region,” *Physical Review Letters*, vol. **28**, 1972.
- [29] M. N. Barber, *Phase Transitions and Critical Phenomena*. Academic Press London, 1983, vol. **8**.
- [30] U. Wolff, “Collective monte carlo updating for spin systems,” *Phys. Rev. Lett.*, vol. **62**, 1989.
- [31] W. Krauth, *Cluster Monte Carlo Algorithms*, in *New Optimization Algorithms in Physics*, edited by A. K. Hartmann and H. Rieger. Wiley-VCH, 2004.
- [32] A. W. Sandvik, “Computational studies of quantum spin systems,” *AIP Conference Proceedings*, 2010.
- [33] L. D. Landau, “On the theory of phase transitions,” *Zh. Eksp. Teor. Fiz.*, vol. **7**, 1937.
- [34] L. D. Landau and E. M. Lifshitz, *Statistical Physics*. Elsevier, 2013.
- [35] M. Abramowitz, *Handbook of Mathematical Functions, With Formulas, Graphs, and Mathematical Tables*, Dover Publications, Inc., 1974.
- [36] T. H. Cormen, C. E. Leiserson, R. L. Rivest, and C. Stein, *Introduction to Algorithms, Third Edition*. The MIT Press, 2009.
- [37] J. Cardy, *Finite-size Scaling*. Elsevier, 2012.
- [38] L. De Sanctis and F. Guerra, “Mean field dilute ferromagnet: High temperature and zero temperature behavior,” *J. Stat. Phys*, vol. **132**, 2008.
- [39] C. Baillie, W. Janke, D. A. Johnston, and P. Plecháč, “Spin glasses on thin graphs,” *Nuclear Physics B*, vol. **450**, 1995.